

Copyright

by

Jie Qiao

2001

**The Dissertation Committee for Jie Qiao
Certifies that this is the approved version of the following dissertation:**

**DENSE WAVELENGTH DIVISION MULTIPLEXING (DWDM)
FOR OPTICAL NETWORKS**

Committee:

Ray T. Chen, Supervisor

Michael F. Becker

Dim-Lee Kwong

George Cardwell

William W. Morey

Dedication

This dissertation is dedicated to my parents for their love,
encouragement, and support

**DENSE WAVELENGTH DIVISION MULTIPLEXING (DWDM)
FOR OPTICAL NETWORKS**

by

Jie Qiao, B.S.,M.S.

Dissertation

Presented to the Faculty of the Graduate School of
The University of Texas at Austin
in Partial Fulfillment
of the Requirements
for the Degree of

Doctor of Philosophy

THE UNIVERSITY OF TEXAS AT AUSTIN

August 2001

Acknowledgements

I have the utmost gratitude to my advisor, Dr. Ray T. Chen, for his constant mentoring and supervision on my research work; also for his positive guidance and motivation in my career preparation. I would like to thank the following faculty members: Dr. Michael F. Becker, Dr. George Cardwell, Dr. Dim-Le Kwong, Dr. Russell Dupuis, and Dr. Joe Campbell, all of the Department of Electrical and Computer Engineering for their excellent teaching, especially thank the first three's valuable time that they have spent serving as my committee members. I also would like to thank Dr. William W. Morey for devoting the time to serve as one of my committee members.

I want to thank my Optical Interconnect group members, Dr. Feng Zhao, Dr. Bipin Bihari, Xuegong Deng, Wei Jiang, Jeff Zou, Xuliang Han, Dechang An, and Yihong Chen, for their assistance and cooperation. Special thanks go to James W. Horwitz of Radiant Photonics Inc, for his contributions to the subject of thermal analysis in Chapter 5, and for his many beneficial discussions on optical design as well.

Finally, special appreciation goes to my parents in China for their love, care, and continuous encouragement on my academic pursuit; and to my brother Jun Qiao for his companionship and support.

Dense Wavelength Division Multiplexing (DWDM) for Optical Networks

Publication No. _____

Jie Qiao, Ph.D

The University of Texas at Austin, 2001

Supervisor: Ray T. Chen

Dense wavelength division multiplexing has become a preferred technique for increasing the information-carrying capability of optical networks by making full use of the huge bandwidth available in optical fibers. In this approach, hundreds of optical channels are multiplexed at the transceiver end and separated at the receiving end, each operating at peak electronic speed. This dissertation focuses on grating-based DWDM, including holographic grating and ruled diffraction grating. Two eight-channel multimode grating-based DWDMs were designed and fully packaged. One of them utilized holographic grating; the other deployed a 22nd order echelle grating and had a thermally optimized optical design. The thermal responses of grating-based DWDM are analyzed and the solution for achieving athermal devices is given. Two ruled diffraction grating-based 32-channel DWDMs were fabricated and demonstrated. Both of them had low, uniform insertion loss; the typical crosstalk was better than -50dB for the single

mode device. Finally the improved optical design and realization of passband broadening, and nonlinear correction of gratings' angular dispersion are described.

Table of Contents

Chapter 1: Introduction to Optical Networks and DWDM	1
1.1 Optical networks	1
1.2 Application of DWDM in optical networks	2
1.3 WDM network architectures	4
1.4 Approaches to multiplexers (MUXs) / demultiplexers (DEMUXs)	5
Chapter 2: The Principle, Design, and Fabrication of Photopolymer-Based Volume Transmission Holographic Gratings.....	17
2.1 Coupled wave theory.....	17
2.2 Recording parameter calculation and experimental setup.....	20
2.3 Holographic grating formation in DuPont photopolymer films.....	22
Chapter 3: Eight-Channel Dispersion-Enhanced Volume Holographic Grating- Based Dense Wavelength-Division Demultiplexer	28
3.1 The grating design principle and the device structure.....	29
3.2 Device packaging and performance	33
3.3 Summary of Chapter 3	35
Chapter 4: Athermalized Low-Loss Echelle Grating-Based Multimode Dense Wavelength Division Demultiplexer	43
4.1 High-order echelle grating design principle and parameters	44
4.1.1 Calculation of desired diffraction order	44
4.1.2 Diffraction angle and angular dispersion calculation.....	46
4.2 Device configuration and optical design details	47
4.3 Simulation for the tolerance of image shift.....	50
4.4 High data transmission bit rate.....	51
4.5 Device performance	53
4.6 Summary of Chapter 4	55
Chapter 5: Thermal Analysis and Compensation of Grating-Based Wavelength Division Demultiplexers.....	69
5.1 Effects caused by the various parts	69
5.2. Center wavelength shift.....	71
5.2.1 Effect of grating thermal expansion	71
5.2.2 Effect of fiber mount in direction of dispersion	73
5.3 Image shift caused by thermal effect.....	75
5.3.1 Effects in the vertical direction	75
5.3.2 Effect in the lateral direction	78
5.4. Change in lens focus	79
5.5 Chapter 5 Summary.....	81

Chapter 6: 32-Channel 100-GHz Echelle Grating-based Demultiplexers	85
6.1 A 32-channel 100 GHz single-mode-in, multimode-out DWDM	86
6.1.1 Device configuration and optical design	86
6.1.2. Demultiplexer Packaging and Performance	87
6.1.3 Simulation and experimental results of the fiber array’s lateral movement tolerance	90
6.1.4 Non-linearity performance of the device when working at ITU standard wavelength	90
6.2 A 32-channel 100 GHz single-mode-in, single-mode-out DWDM	91
6.2.1 Device structure and optical design	91
6.2.2 Device performance	92
6.3 Chapter 6 Summary	94
Chapter 7: Optimized Optical Design for Passband Broadening and Nonlinear Correction of Angular Dispersion	109
7.1 Passband broadening	109
7.2 Design of Graded-index lensed fibers (GILFs)	111
7.3 Cylindrical lens for passband broadening	113
7.4 40-Channel single-mode demultiplexer using a thermally-diffused expanded-core fiber array with uniform spacing	115
7.5 Chapter 7 Summary	117
References	130
Vita	144

Chapter 1: Introduction to Optical Networks and DWDM

1.1 Optical networks

The tremendous growth of the Internet and other data, image, voice services is driving the need for more and more bandwidth in networks. The bandwidth of one single-mode optical fiber is about 25 THz in the 1.5 μm band alone. Optical networks, having optical layer as the dominant technology for transport, becomes a key technology to fulfill the demands for bandwidth.

Optical networks can be opaque or all optical. In opaque networks the optical-electronic-optical (OEO) conversion operation interrupts the path between end users at intermediate nodes. The optical layer resides under existing layers such as the traditional synchronous optical networks (SONET) or synchronous digital hierarchy (SDH). This multiple layers can significantly reduce network equipment cost and make it work more efficiently. Usually, SONET and SDH layers are used to process smaller amounts of bandwidth at a finer level. Optical layers process large amounts of bandwidth at a relatively coarse level [1].

In all-optical networks, each light path is completely optical, or at least totally transparent, except at the end nodes [2]. There are three major reasons that human want to go to all-optical networks: Most apparent is the huge bandwidth available in optical fibers. The fiber bandwidth is mined by deploying dense wavelength division multiplexing (DWDM), increasing the information carrying capability of optical networks by transmitting multiple highly resolved wavelengths on the same fiber.

The second reason is that there is totally no protocol dependency in all-optical wavelength division multiplexing (WDM) light path; different channels may have different bit rate and formats. The third advantage is the functional simplicity and low cost. All-optical networks do not require OEO conversion, making the transmission more efficient and cost-effective. The maintenance is also much simpler than that of traditional fiber-plus-OEO systems.

1.2 Application of DWDM in optical networks

The main function of WDM is to combine two or more wavelengths into a single fiber at the transceiver end. The separation of these wavelengths takes place at the receiver end by deploying different demultiplexing techniques. When the wavelength spacing is less than 1nm, it is defined as DWDM. DWDM increases the capacity of embedded fiber by dividing the incoming optical signals into a number of non-overlapping frequency bands and then multiplexing the resulting signals out onto one fiber [3] (Figure 1.1). The combined multiple optical signals can be amplified as a group and transported thousands of miles on an optical fiber. DWDM effectively multiplies the capacity of a single optical fiber by a factor of 160 or more. Utilizing WDMs in optical networks can achieve link capacities on the order of 50THz.

Because incoming signals are never terminated in the optical layer, the interface can be bit-rate and format independent [4]. DWDM can carry individual signals at a different rate (OC-48/192, etc.) and in a different format (SONET, SDH, ATM, data, etc.). For instance, a DWDM network with a mix of SONET signals operating at

OC-48 (2.5 Gbps) and OC-192 (10 Gbps) over a DWDM infrastructure can achieve capacities of over 40 Gbps. As a method of leveraging unused capacity in existing embedded fiber, DWDM technology is easy to integrate into existing networks because the optical layer is bit and format independent. DWDM also offers several alternate channels to link various nodes and is therefore more resilient to channel failure [5].

The invention of erbium doped fiber amplifiers (EDFA's) enable to amplify signals in a band of frequencies, rather than individually. Therefore the maximum number of channels of DWDM is directly related to the bandwidth of EDFA's. Ultra wideband EDFA's have become available with a bandwidth of 80 nm, approximately 7 times the bandwidth of standard EDFA (1528-1568nm) [6]. Using this ultra wideband amplifier, 100 channels were transmitted over a distance of 400 km with a data rate of 10 Gbps/channel [7] with a system capacity of 400 Tbps km. On the other hand, more than 1000 optical channels have been multiplexed in a fiber by using a single laser [8]. This trend is expected to continue further.

But DWDM is really just the first step to all-optical networks. We also need to have all-optical add-drop multiplexers (OADMs) to fully access to traffic at different nodes optically. OADM selectively drops a wavelength from a multiplicity of wavelengths in a fiber, and thus the information carried on this wavelength. Then it adds the same wavelength, carrying different data content, in the same direction of data flow. The all-optical crossconnects (OXC's) act as a large photonic switch, which gives networks the ultimate bandwidth management flexibility. An OXC has N full-

duplex ports, each of which can connect to any other and also itself. Only combining OXCs, DWDMs, and OADMs together, we can realize flexible, efficient, configurable, and high-capacity optical networks with full optical bandwidth management.

1.3 WDM network architectures

WDM network architectures can be classified into two broad categories: broadcast and select architectures and wavelength routing architectures [1,9].

Broadcast and select WDM networks enable the sharing of information among nodes. Figure 1.2 shows this structure. The sharing medium here is a star coupler; bus topologies and ring topologies are also common. The star coupler combines and broadcasts all the signals transmitted by different nodes. Each output node receives a fraction of power from each signal. Wavelength selection can be realized using tunable receivers at different nodes. However, protocols are needed to determine the corresponding wavelength that individual nodes can receive. This form of a network is simple and suitable for use in local or metropolitan area networks, such as access networks. Because the wavelength cannot be reused in the network, and transmitted power from a node must be split among all the receivers in the network, the number of nodes in these networks is limited. A number of broadcast and select testbeds [10-14] have been developed by various research laboratories. Primarily, these demonstrate circuit switching rather than packet switching.

Figure 1.3 gives a wavelength routing network, in which information is routed, switched, and forwarded based on wavelength. Compared to broadcast-and-select networks, wavelength routing networks are more sophisticated and practical. This architecture does not suffer from the splitting loss caused by broadcasting the power to unwanted receivers. The nodes in the networks are capable of routing different wavelength at one input port to different output ports. These networks also allow spatial reuse of wavelength, *i.e.*, many simultaneous lightpaths using the same wavelength can be set up. Thus wavelength routing networks are suitable for deployment in metropolitan- and wide-area networks, such as local-exchange and interchange networks.

1.4 Approaches to multiplexers (MUXs) / demultiplers (DEMUXs)

At this time, several competing technologies for making MUXs/DEMUXs are being actively developed [15]. These technologies include multiplayer dielectric thin-film filters, Bragg grating filters [16-21], phased-array-waveguide-gratings [22-28], and diffraction gratings[29-33]. The important characteristics of WDMs used in telecommunications systems are insertion loss, polarization dependent loss (PDL), temperature effect, passband flatness, crosstalk, packaging size, and cost.

Thin-film dielectric devices are the most broadly deployed filters for low-channel-count DWDM systems in the 400- and 200-GHz channel spacing regime. As Fig. 1.4 shows, two or more resonant cavities are separated by reflective dielectric thin-film layers, which have quarter-wave thickness, and alternating high and low indices.

These resonant cavities form a bandpass filter, transmitting a specific wavelength and reflecting all other wavelengths. This mature technology offers good temperature stability ($<0.002 \text{ nm}/^\circ\text{C}$), channel-to-channel isolation, and a flat passband. It's primary challenge is to decrease the channel spacing to 100 GHz and below, with good yield, as well as increasing the channel count beyond 16.

The principle of array waveguide gratings (AWGs) is interferometry. Fig.1.5 shows the structure of an array waveguide WDM [34]. The wavelength-dependent phase delays are caused by the length differences of the arrayed waveguides. The varies wavelengths with different phase interfere with each other in such a manner that each wavelength achieve maximum energy at a designed position. The separated wavelengths can be coupled into a fiber array. Since AWGs are fabricated using stander IC technologies, these devices lend themselves to high integration and consequently large channel counts. Channel spacings are typically 100 GHz, although 50 GHz devices are also available. But temperature stability is often a concern, requiring active temperature controller.

The dispersion of fiber Bragg grating is achieved by periodically varying the index of refraction of a fiber segment. Fig.1.6 shows how the fiber gratings are made. The periodic variation of index is formed by exposing the germano-silicate core of the fiber to an intense periodic ultra-violet (UV) pattern.

Insertion loss and uniformity of fiber Bragg grating based devices are very good because they are fabricated from standard single-mode fiber. The long-term stability is an issue due to the stability of tuning.

Diffraction-grating devices feature a finely ruled grating that diffracts the incident beam into different angles and positions. As shown in Fig. 1.7, each wavelength channel corresponds to a unique diffraction angle and can be collected by individual fibers. This technology has several major advantages, including low and uniform insertion loss across the entire passband, superior crosstalk, accurate wavelength, and athermal performance. It is also scalable: lower channel count devices can be upgraded to higher count devices simply by installing more fibers. Table 1.1 [35] gives a comprehensive comparison among those technologies for making MUXs/DEMUXs.

The research work presented in this dissertation focuses on diffraction grating-based DWDM. The overall objective of this dissertation was to design and build MUXs/DEMUXs with good performance for local, metropolitan, and backbone area networks. The good performance includes low insertion loss (Less than 3dB for low channel count multimode MUXs, less than 6 dB for 32 channel single-mode MUXs), low crosstalk (lower than -30 dB), and good thermal performance, *i.e.*, minimizing the central wavelength, insertion loss shift across the temperature range 20-60°C. The data transmission bit rate should be higher than 2.5 Gbps for multimode devices, and higher than 10 Gbps for single-mode devices.

In Chapter 2, coupled wave theory related to transmission holograms, and the fabrication of holographic gratings will be presented. A fully packaged eight-channel dispersion-enhanced volume holographic grating based DWDM is described in Chapter 3, Chapter 4 presents an athermalized low-loss echelle grating-based eight-channel multimode DWDM. Chapter 5 analyzes the thermal responses of different parts of diffraction grating-based DWDMs, and presents the means of achieving athermalized WDM devices. In Chapter 6, two fully packaged 32-channel DWDMs are demonstrated. One of them was designed for metropolitan area networks; the other was designed for long-haul telecommunications networks. Chapter 7 proposes various means of broadening the optical passband of grating-based DWDMs; the optimized design for non-linear correction of angular dispersion is then presented.

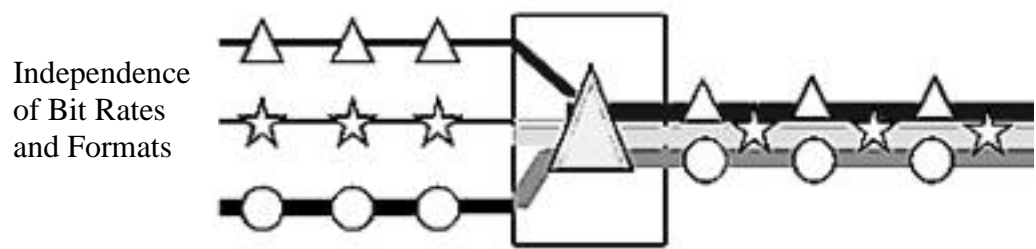


Fig 1.1 Increased Network Capacity by using WDMs [3].

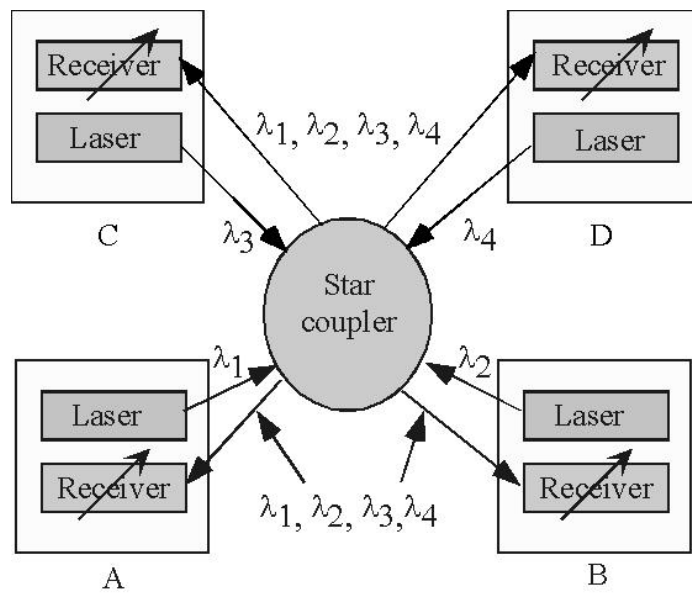


Fig. 1.2 A WDM broadcast and select network

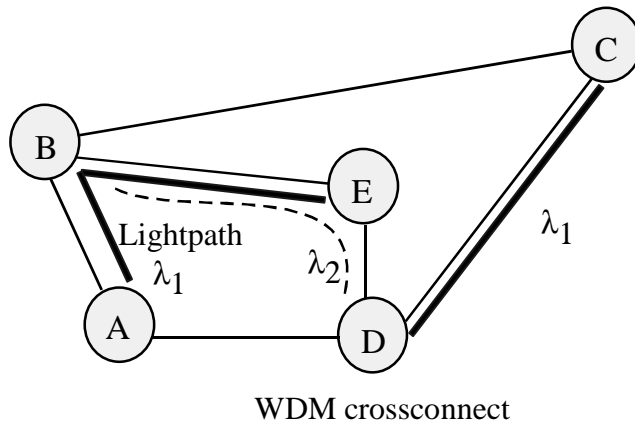


Fig.1.3 WDM wavelength routing network

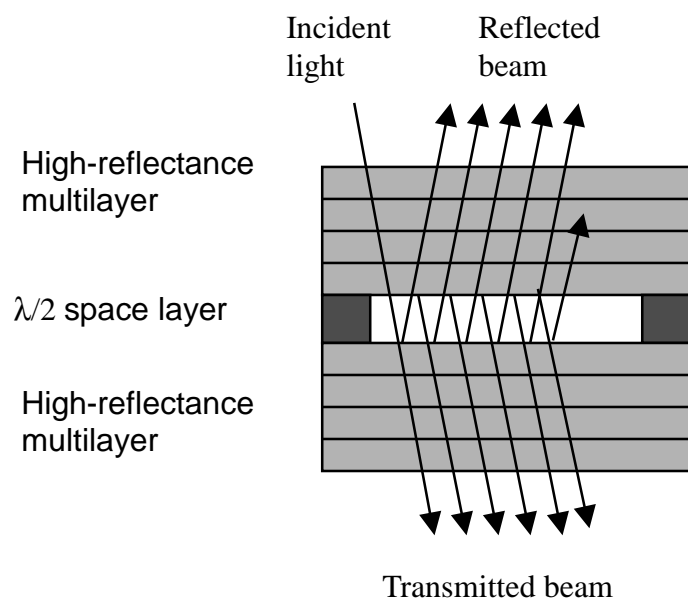


Fig.1.4 Interference filter [34]

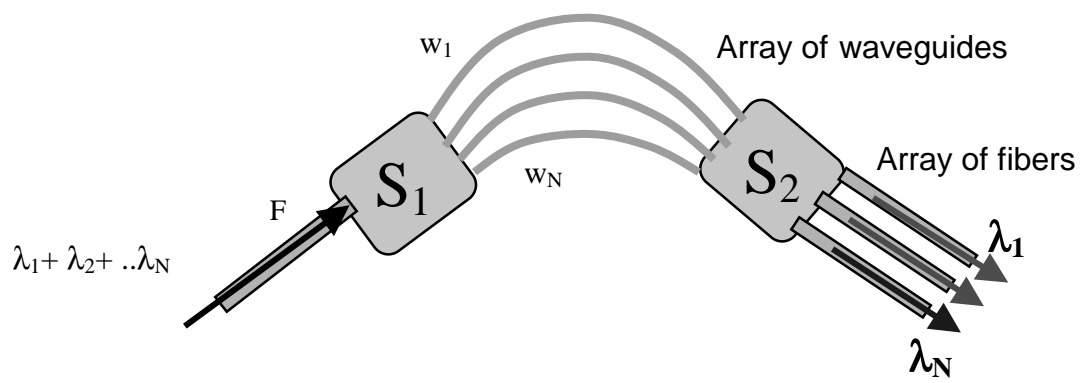


Fig. 1.5 Array waveguide grating [34]

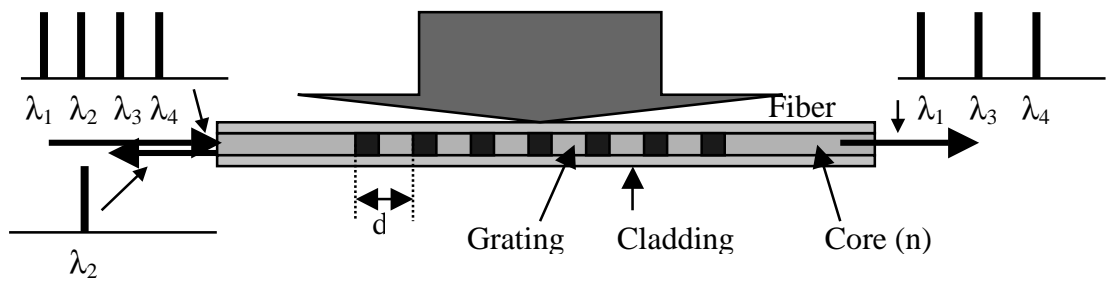


Fig. 1.6 A fiber is exposed under UV light to create index modulation [34].

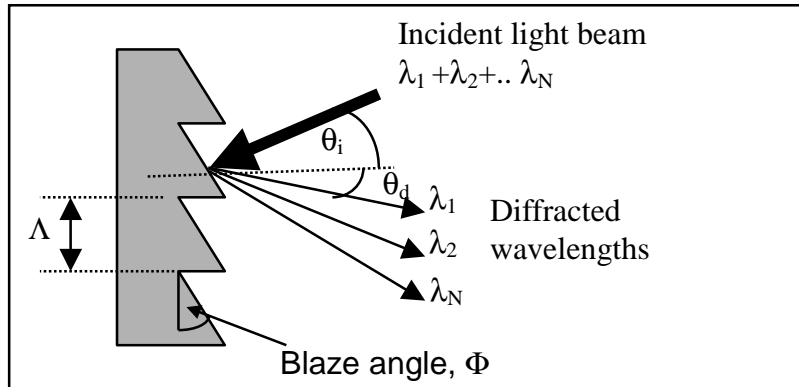


Fig.1.7 Diffraction grating based WDM; different wavelength is diffracted into different angles and positions

Table1.1 Comparison among various technologies for making DWDMs [35]

Technologies	Advantages	Disadvantages
Thin-film dielectric interference	<p>Mature technology</p> <p>Good temperature stability</p> <p>Good wavelength selectivity</p> <p>Very good PDL</p> <p>Flat passband</p>	<p>Difficult to product narrow channel spaced filters (<100GHz)</p> <p>Insertion loss is not uniform for high channel counts</p> <p>Filters can only be manufactured for a fixed wavelength</p> <p>Not scalable</p>
Planar array Waveguide	<p>Uses IC fabrication processes.</p> <p>Scalable to high channel counts</p> <p>Can integrate multiple functions on a single chip</p>	<p>Difficult fiber interface</p> <p>Capital-intensive</p> <p>Requires large infrastructure</p> <p>Need temperature controller</p>
Fiber Bragg Gratings	<p>Mature technology</p>	<p>Mechanical stability problem</p> <p>High back reflection; must use isolator.</p>
Fused, cascaded Mach-Zehnder Interferometers	<p>Low insertion loss and polarization effects</p> <p>Can produce very narrow channel spaced devices</p> <p>Easy coupling to fiber</p> <p>Generates filter “comb” rather than wavelength-specific filter</p>	<p>High channel count devices require cascaded devices resulting in a larger form factor device.</p>
Diffraction Gratings	<p>Low & uniform insertion Loss</p> <p>Best crosstalk, less than -40dB</p> <p>Good temperature stability</p> <p>Scalable</p>	<p>Devices can be bulky</p> <p>Typically used in a free space mode requiring careful assembly techniques.</p>

Chapter 2: The Principle, Design, and Fabrication of Photopolymer-Based Volume Transmission Holographic Gratings

2.1 Coupled wave theory

When analyzing diffraction mechanism of thick holographic gratings, one can think in this way that the amplitude of the incident wave decreases while propagating through the gratings, whereas that of the diffracted wave increases progressively. One way to analysis this is by means of a coupled-wave approach [36-38]. The remainder of this section outlined Kogelnik's coupled-wave theory [39].

Here, we only take into account the incoming reference wave R and the outgoing signal wave S which obey the Bragg condition; the other diffraction orders are neglected because they violate the Bragg condition strongly.

Figure 2.1 shows the model of a holographic grating, which was used for the analysis. The x -axis is parallel to the medium boundaries and in the plane of incidence, the y -axis perpendicular to the paper, and the z -axis is perpendicular to the surfaces of the medium. The grating fringes are slanted with respect to the medium boundaries at an angle Φ . The grating vector, $K=2\pi/\Lambda$, is perpendicular to the fringes, where Λ is the period of the grating. The incident angle in the medium is θ_i . Wave propagation in the grating is described by the scalar wave equation

$$\nabla^2 E + k^2 E = 0, \quad (2.1)$$

where $E(x,z)$ is the complex amplitude of the y-component of electric field, which is assumed to be independent of y. The propagating constant $k(x,z)$ is spatially modulated and can be calculated by Eq. (2.2)

$$k^2 = \beta^2 - 2j\alpha\beta + 2\kappa(e^{jK \cdot x} + e^{-jK \cdot x}), \quad (2.2)$$

where,
$$\beta = 2\pi n / \lambda; \quad \alpha = \mu c \sigma_0 / 2\sqrt{\epsilon_0}, \quad (2.3)$$

ϵ_0 is the average dielectric constant; σ_0 is the average conductivity; c is the light velocity in free space, and μ is the permeability of the medium.

When the modulation is small, the coupling constant κ describing the coupling between the reference wave R and the signal wave S can be expressed as Eq. (2.4)

$$\kappa = \pi n_1 / \lambda - j\alpha_1 / 2. \quad (2.4)$$

The spatial modulation indicated by n_1 and α_1 causes the coupling and the energy exchange between the waves R and S . If $\kappa=0$, there is no coupling between R and S ; therefore, there is no diffraction. The total electric field in the grating is the superposition of the two waves:

$$E = R(z)e^{-j\rho \cdot x} + S(z)e^{-j\delta \cdot x} \quad (2.5)$$

Figure 2.2 shows phase matching condition among the propagation vectors ρ , δ and the grating vector K .

$$\vec{\delta} = \vec{\rho} - \vec{K}. \quad (2.6)$$

When the Bragg condition is satisfied, the lengths of both ρ and δ are equal to the free propagation constant β .

$$\cos(\phi - \theta) = K / 2\beta \quad (2.7)$$

The amplitude of a wave changes along z because of coupling to the other wave (κ_R, κ_S) or absorption (α_R, α_S). The transmitted or reflected wave amplitude can be obtained by applying the boundary condition. For transmission volume holographic gratings, the boundary conditions are $R(0) = 1$ and $S(0) = 0$, where $c_s > 0$. For an s-polarized optical signal, the diffraction efficiency is

$$\eta_s = \frac{\sin^2(\gamma_s^2 + \xi^2)^{\frac{1}{2}}}{(1 + \xi^2 / \gamma_s^2)}, \quad (2.8)$$

where

$$\gamma_s = \frac{\kappa_s d}{(c_R c_s)^{1/2}} \quad (2.9)$$

$$\xi = \frac{\Delta\theta \cdot K d \sin(\phi - \theta)}{2c_s} = \frac{\Delta\lambda \cdot K^2 d}{8\pi n c_s} \quad (2.10)$$

$$\kappa_s = \frac{\pi \Delta n}{\lambda}, \quad (2.11)$$

$$c_R = \cos\theta, \text{ and } c_s = \cos\theta - \frac{K}{\beta} \cos\phi \quad (2.12)$$

For a p-polarized input optical signal, the above equations can be used again by replacing κ_s in Eq. (2.8) with

$$\kappa_p = -\kappa_s \cos 2(\theta - \phi) \quad (2.13)$$

where γ and ξ are real-valued and d is the thickness of emulsion.

The diffraction efficiency can be controlled by intensities of recording beams in the formation of recording holographic gratings, since γ is dependent on only index modulation with given reconstruction wavelength,

2.2 Recording parameter calculation and experimental setup

The hologram was fabricated in-house by a two-beam interference method (Figure 2.3). The hologram material was DuPont photopolymer HRF 600X001-20 (20 μm thick) made by DuPont (DuPont Holographic Materials, Wilmington, Delaware). A Verdi Laser was operated in single wavelength (532 nm). A beam coming from the laser was divided into two by a beam splitter and then collimated by two sets of collimators. Light attenuators adjust the intensity of the two beams. The objective lenses expand the laser beams, followed by spatial filters at their focal points to eliminate scattering light. A piece of holographic material was mounted on a rotational stage. One collimated beam directly illuminated the hologram while a mirror deflected the other beam. The holographic material was exposed to the interference pattern of two collimated laser beams. The two beams interfered and created a periodic structure of refractive index modulation inside the hologram.

The two recording angles, α_1 and α_2 , can be set by tuning the relative positions and angles of the rotation stage and the mirror. The slant angle ϕ of the grating and the grating period Λ are given by [40]

$$\Phi = \frac{\pi}{2} + \frac{\theta_{dh} - \theta_{ih}}{2}, \quad (2.14)$$

and

$$\Lambda = \frac{\lambda_{rc}}{2n \sin\left(\frac{\theta_{dh} + \theta_{ih}}{2}\right)}, \quad (2.15)$$

where, λ_c , λ_{rc} are the wavelengths of the recording beam and the reconstruction beam respectively. θ_{ih} and θ_{dh} are the incident angle and the diffraction angle of the optical signals in the holographic grating region at the center wavelength of λ_{rc} ; $n=1.52$ is the average refractive index of the holographic grating region. Figure 2.4 shows that the grating vector \mathbf{K} ($|\mathbf{K}| = 2\pi / \Lambda$) is phase-matched with the recording wave vector \mathbf{k}_c ($|\mathbf{k}_c| = 2\pi n' / \lambda_c$), and with the reconstruction wave vector \mathbf{k}_{rc} ($|\mathbf{k}_{rc}| = 2\pi n / \lambda_{rc}$). The average refractive index of the guided-wave holographic emulsion at recording wavelength λ_c is n' . The angle between recording beams in the hologram medium at wavelength λ is given by

$$\beta = 2 \sin^{-1} \left(\frac{n\lambda_c}{n'\lambda_{rc}} \sin(\theta_{dh} + \theta_{ih}) \right) \quad (2.16)$$

The recording angle inside the holographic grating can be calculated by Eqs. (2.17), and (2.18)

$$\alpha_{1h} = \pi / 2 - (\phi - \beta / 2), \quad (2.17)$$

$$\alpha_{2h} = (\phi + \beta / 2) - \pi / 2, \quad (2.18)$$

The recording angles in the air can be calculated by Snell's Law:

$$\alpha_1 = \sin^{-1}(n' \sin \alpha_{1h}) \quad (2.19)$$

$$\alpha_2 = \sin^{-1}(n' \sin \alpha_{2h}) \quad (2.20)$$

When incident angle $\theta_{\text{in}}=60^\circ$, diffraction angle $\theta_{\text{dh}}=34.7^\circ$, the calculated recording beam angles in the air are $\alpha_1=44^\circ$ and $\alpha_2=-2^\circ$.

2.3 Holographic grating formation in DuPont photopolymer films

DuPont photopolymers are promising holographic films due to their dry processing, long shelf life, good photo-speed, and large index modulation [41-44]. The holographic photopolymer is spin coated from solvent on a clear support, typically Mylar polyester film. A removable cover sheet is used as a protecting cover. The thickness of the photopolymer film is available from 10 to 100 μm .

The formation mechanism of holographic grating in photopolymer films is known to be a three-step process [40]. First, an exposure initiates the interference pattern, which causes initial polymerization and diffusion of the monomer molecules to bright fringe areas from the dark fringe neighborhoods in the photopolymer. A higher concentration of polymerization means a higher refractive index. Second, a uniform UV light is required for dye bleaching and complete polymerization. Third, a baking process can further enhance the refractive index modulation of the hologram formed in the photopolymer film.

The dynamic range of the diffraction efficiency versus exposure time is related to the polymerization rates and the diffusion rates, which can be controlled by the intensities of the two recording beams. Assuming the ratio of the two recording beam intensities is 1:1, before saturation, if the intensities of the two recording beams are too low, the polymerization rates in both dark and bright fringes will be relatively

low, therefore, the diffraction efficiency increases at a very low speed. On the other hand, if the intensities of the two recording beams are too high, the polymerization rates will be larger than the diffusion rates in the dark fringe regions, thus the resulting diffraction efficiency shows a decrease when the diffusion processing is stopped by rigidity in the in the polymerized portion of the film. It is important to have optimum recording intensity to achieve monomer diffusion rates compatible with the polymerization rates in the dark fringe regions of the photopolymer film. In this case, a smoothly increasing diffraction efficiency curve with a saturation region can be obtained.

In our experiment, DuPont HRF 600X001-20 (20 μm thick) was selected as the recording material because it exhibits lower scattering and higher diffraction efficiency [44]. The ratio of the recording beam intensities was 1:1.2. The laser power was 5mW. The optimum exposure time was 60s for reconstruction wavelength of 1550 μm . After recording, the hologram was UV-cured for three minutes. Then it was baked for two hours at 100°C.

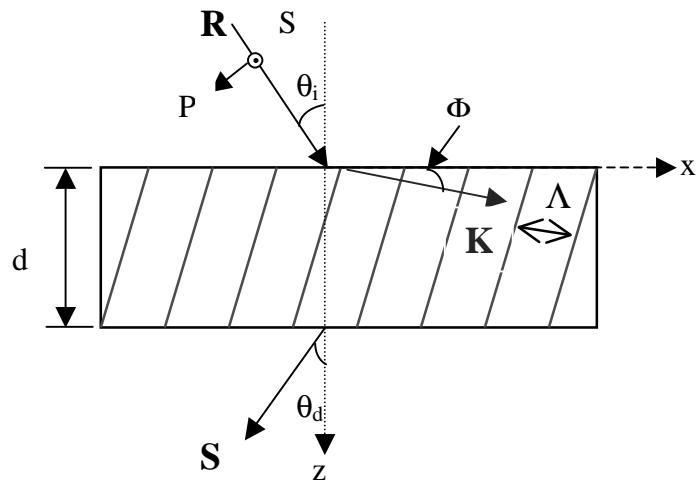


Fig. 2.1 Model of a thick holographic grating with slanted fringes.

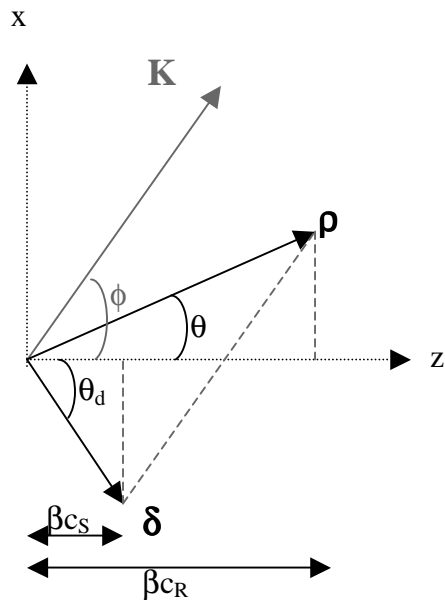


Fig. 2.2 Propagation vectors of the input wave, output wave, and grating vector.

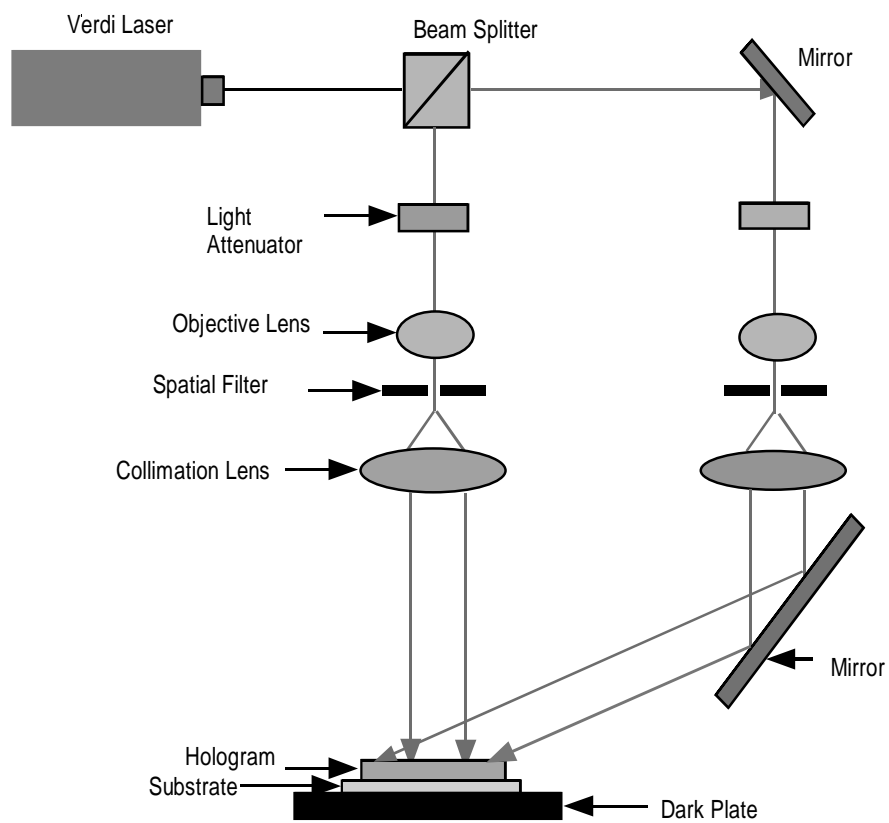


Fig. 2.3 Experimental setup for recording volume holograms using the two-beam interference method

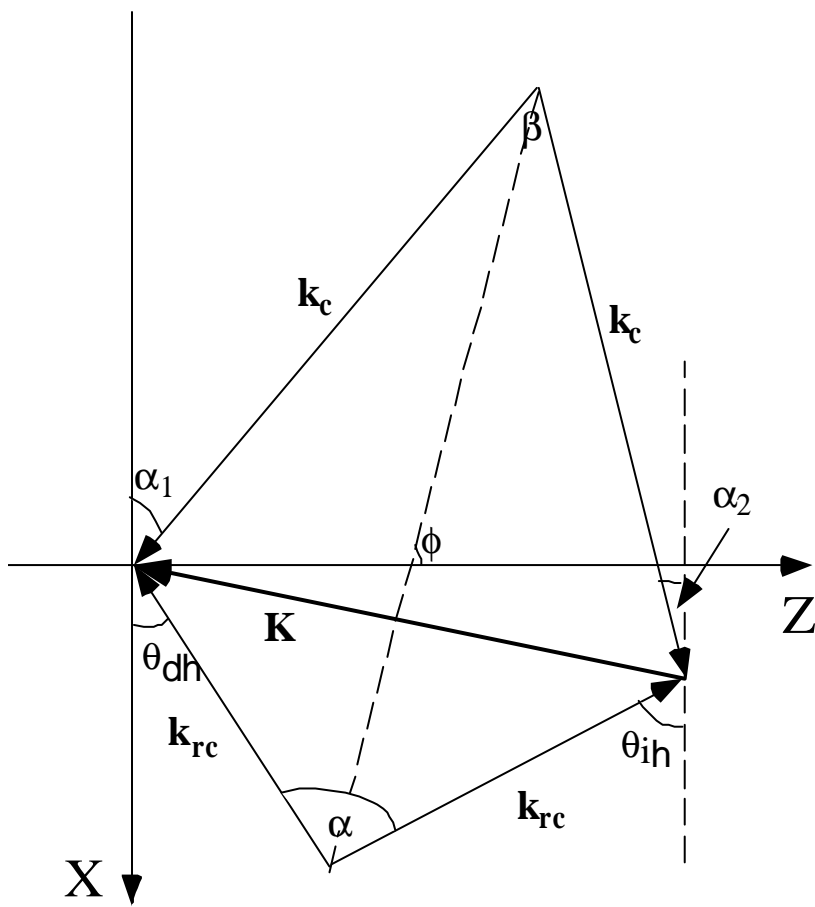


Fig. 2.4 Phase matching condition for recording and reconstruction of the grating

Chapter 3: Eight-Channel Dispersion-Enhanced Volume Holographic Grating-Based Dense Wavelength-Division Demultiplexer

For long-haul telecommunications and data communication in metropolitan areas at wavelengths of 1330 nm and 1550 nm, WDM technologies have been focusing on Bragg grating [16-21] and arrayed waveguide gratings (AWG) [22-28]. Holographic gratings have been extensively deployed in integration optics and optical interconnects due to their flexible design and fabrication capability [45-52]. In this chapter, an eight-channel fully packaged dense wavelength division demultiplexer (DWDDM) is presented (Sections 3.1 and 3.2) which employs a novel dispersion-enhanced grating design [53], using a path-reversed substrate-guided-wave configuration working at a center wavelength of 1555 nm [54]. The polymer-based holographic grating [55-62] lowers the cost of the device compared to using gratings made from other materials. Multi-mode fibers enable the demultiplexer to resist mechanical and environmental disturbance well. The lights are zigzagged within a wedge-angled substrate, decreasing the device's size effectively. This demultiplexer is not only compact in size, but also reliable in operation and more cost-effective compared with counterparts using other methods [16-28].

3.1 The grating design principle and the device structure

A path-reversed photopolymer-based substrate-guided holographic grating is used for demultiplexing eight wavelengths with 2 nm separations. The particular choice of wavelengths and wavelength channel spacing is due to the requirements of the parallel optical interconnect system built by the Jet Propulsion Lab [63].

Figure 3.1 shows the structure of the substrate-guided-wave interconnect scheme. Collimated optical signals with different wavelengths are coupled into a waveguiding plate with an aluminum-coated beveled edge of an angle α , zig-zagged within the substrate with a bouncing angle larger than the critical angle of the waveguiding plate, and then coupled out by the photopolymer-based volume holographic grating fabricated on one side of the substrate. The dispersed optical signals can be coupled by a focusing lens into a fiber array. The thickness of the waveguiding plate is t . Figure 3.2 shows the detailed structure of a volume holographic grating with a thickness of d . The grating has a period of Λ and a slant angle of ϕ . The grating equation is given by [36]

$$\Lambda_y (\sin\theta_{dh} + \sin\theta_{in}) = m \lambda / n , \quad m = 0, \pm 1, \pm 2, \dots \quad (3.1)$$

where θ_{in} and θ_{dh} are the incident angle and the diffraction angle respectively of the optical signals in the holographic grating region at the center wavelength of λ (in the air). The average refractive index of the holographic grating region is n .

$\Lambda_y = \Lambda / \sin \phi$ is the grating period projected in the direction Y. The m th forward diffraction order is represented by m . In our case, $m = 1$. Let θ_{diff} be the designed

diffraction angle in the air of refractive index n_3 , and let θ_{in} be the bouncing angle, i.e., the incident angle at the interface between the waveguiding plate and the grating. From the geometrical layout of the beveled edge, we have $\theta_{in} = 2 \alpha$

The dispersion of the grating can be derived by differentiating Eq. (3.1), giving

$$\begin{aligned} d\theta_{diff}/d\lambda &= \sin\phi / \Lambda \cos\theta_{diff} \\ &= n (\sin\theta_{dh} + \sin\theta_{in}) / \lambda \cos\theta_{diff}. \end{aligned} \quad (3.2)$$

From Equation 3.2, one can easily conclude that the larger the diffraction angle, or the larger the incident angle, the greater the angular dispersion. The larger the angular dispersion, the smaller the packaging size. Consequently, large angular dispersion is always preferable in DWDM design.

For grating design, the spectral bandwidth of the grating is also a quite important parameter, which has to accommodate all wavelength channels demultiplexed. The approximate spectral bandwidth is given by Ludman [64] in the form of

$$\Delta\lambda / \lambda = \Lambda \cos\theta_{dh} \sin\phi / d \sin\theta_{dh}, \quad (3.3)$$

which indicates that the larger the diffraction angle, or the larger the incident angle, the smaller the bandwidth. There exists a trade-off between the dispersion and the bandwidth of the guided-wave holographic gratings.

The diffracted multi-wavelength signals are coupled into a silicon V-grooved multimode fiber array with a 62.5 μm diameter core, and a 250 μm channel-to-channel

spacing. The linearity of the angular dispersion among different wavelengths is critical for achieving balanced coupling efficiency. Since the channel spacing of the multimode fiber array in the experiments under discussion is exactly 250 μm , and the required wavelength separation is also uniform (2 nm), we definitely expect to achieve perfect linearity of angular dispersion to meet these two factors. But Equation 3.2 shows that angular dispersion is not a linear function of diffraction angle. The condition for achieving linear angular dispersions among different channels can be found by taking the second-order derivative of the diffraction angle, *i.e.*,

$$\frac{d^2\theta_{diff}}{d\lambda^2} = \frac{\sin(\theta_{diff})}{\cos^3\theta_{diff} \Lambda_y^2}. \quad (3.4)$$

When the diffraction angle in the air is zero, the best angular dispersion linearity can be achieved. The diffraction angle at different wavelengths is

$$\theta_{diff(\lambda)} = \arcsin(\lambda / \Lambda_y - n \times \sin(\theta_{dh})) \quad (3.5)$$

The diffraction angle difference between a specific wavelength and the center wavelength is:

$$\Delta\theta_{diff(\lambda)} = \theta_{diff(\lambda)} - \theta_{diff(center-\lambda)} \quad (3.6)$$

Channel spacing between the specific wavelength and the center wavelength is thus determined to be

$$\Delta d_{(\lambda)} = f \times \tan(\Delta\theta_{diff(\lambda)}) \quad (3.7)$$

In Equation (3.7), f is the focal length of the lens used for focusing the light spot down to diffraction limit. The simulation result of channel spacing deviation at two different incident angles and diffraction angles is shown in Table 3.1. For the incident angle of 60° in the air, the diffraction angle of 0° in the air ($60^\circ / 0^\circ$ structure), we can achieve relatively accurate wavelength, but the dispersion ability is only 0.0485 degree per nanometer. For a grating structure with the incident angle of 60° in the air, the diffraction angle of 60° in the air ($60^\circ / 60^\circ$ structure), the dispersion ability is 0.1600 degree per nanometer, which is 2.3 times greater than that of the $60^\circ / 0^\circ$ structure. But the linearity of its angular dispersion is less satisfactory than that of the $60^\circ / 0^\circ$ structure. Table 3.1 indicates that there exists a trade-off between the dispersion ability and the dispersion linearity. For the $60^\circ / 60^\circ$ structure, most of the channel spacing deviations are smaller than $6\mu\text{m}$. Compared to the core diameter of a multimode fiber and the small light spot size, which is close to diffraction limit. This result is tolerable. The largest deviation is $24.08\ \mu\text{m}$, which can be compensated for by tuning the wavelength slightly at the particular channel. We selected a grating structure with a grating period Λ of 694 nm, a diffraction angle θ_{diff} of 60° in the air and an incident angle θ of 60° in the grating. This structure can provide a relatively large dispersion and bandwidth, $d\theta_{\text{diff}} / d\lambda = 0.16^\circ / \text{nm}$. The beveled edge provides a means of overcoming the limitation of the critical angle inside the waveguiding substrate and to enhance the dispersion of the holographic grating.

3.2 Device packaging and performance

Figure 3.1 illustrates the design layout of the device. A collimator with a single-mode fiber and an FC fiber connector, a computer-optimized achromatic lens, a silicon V-grooved multimode fiber array, and the holders of these parts are integrated on a 4.3×2.7 -inch base plate. The light coming from WDM lasers is transposed to a collimator by a polarization-maintaining single-mode fiber, and is diffracted by a $60^\circ / 60^\circ$ holographic grating. Diffracted beams outside the grating vary almost linearly with the deviation of eight input wavelengths. A lens is used to focus the beams down to diffraction-limited spots, which can be coupled into an eight-channel silicon V-grooved multi-mode fiber array. The device is designed for optical communications for metropolitan-area networks where both free space DWDM and multi-mode fiber band networks are jointly employed [65].

To maintain precision and accuracy during the packaging, the V-grooved fiber array is installed on a specially designed gripper whose positioning can be controlled by a position system with six degrees of freedom including X, Y, Z translation, rotation, pitch, and yaw. Because infrared light is invisible, it becomes critical to locate the exact focal plane of the lens. First, we coupled the center wavelength 1555 nm to the 4th channel of the V-grooved fiber array, which is the channel designed for coupling the center wavelength. The smallest insertion loss and balanced crosstalk to the two neighboring channels can be reached by adjusting the X, Y, and Z translation stage. At this time, the focal point of the lens is immediately on the front face of the

V-grooved fiber array when operating at the center wavelength. Similarly, the other seven wavelengths are coupled to the corresponding channels with the smallest insertion loss and balanced crosstalks.

Epoxy injection and UV curing are used to fix all the optical components on their mounts permanently. There is no observed component displacement after UV curing.

Because WDM laser sources usually contain a spectral width dependent on the laser cavity structures and the operating conditions [66], Laser wavelength shift is also present when the laser is internally modulated [67]. Dispersion non-linearity limits the wavelength range and channel spacing. It was observed that there was an extremely small shift in the coupled wavelength compared to the designed.

The fully packaged device is shown in Figure 3.3. Two terms need to be defined here. *Insertion loss* is defined as the power loss from the pigtail of the WDM laser to the output of the silicon V-grooved fiber array, including the loss of the input signal mode fiber, the collimator, the holographic grating, the lens, and the silicon V-grooved fiber array and its coupling loss. *Crosstalk* is the power difference between a specific channel and its neighbor channels when only that specific channel is on. The measured insertion losses and crosstalk of the DWDDM system are listed in Table 3.2. The typical value of crosstalk is less than -35dB , which is satisfactory for optical communications networks. The typical insertion loss of this system is in the neighborhood of -5.5dB . Grating loss is a major factor in the total insertion loss. The diffraction efficiency of the holographic grating is 40% [53], which is due to the fixed index modulation and film thickness provided by DuPont photopolymers (DuPont

Holographic Materials, Wilmington, Delaware, USA) [68,69] We are trying to use other gratings from other sources which have much higher diffraction efficiency at the required working wavelength. (The diffraction efficiency of grating made by American Holographic, Inc is higher than 97.3% at the wavelength range from 1540 nm to 1570 nm. The diffraction efficiency of gratings made by Optometrics USA is higher than 86% at the wavelength range from 1400 nm to 1600 nm.) The insertion losses can be decreased significantly, down to -1.5 dB to -2.5 dB, by using these gratings. The measured optical 1dB passband is 0.2 nm, which corresponds to the 30 μ m movement range of the fiber array. The wide optical passband makes the device robust to variation in environmental temperature.

Figure 3.4 shows the output spectrum from the eight-channel V-grooved fibers when input wavelengths are 1549, 1551, 1553, 1555, 1557, 1559, 1561, and 1563 nm. The output spectrum was measured by a laser rather than by a wide-band white-light source, so it shows the center wavelength of each individual channel rather than the exact loss spectrum of each channel, because of the narrow line width and uneven input power of the laser.

3.3 Summary of Chapter 3

The DWDDM designed here employed dispersion-enhanced volume holographic gratings and silicon V-grooved multi-mode fiber array with 250 μ m spacing to demultiplex optical signals to eight channels, namely at wavelengths of 1549 nm, 1551 nm, 1553 nm, 1555 nm, 1557 nm, 1559 nm, 1561 nm, and 1563 nm. The

packaging losses of these channels are -5.68, -5.6, -5.40, -5.3, -5.68, -5.59, -5.58, and -5.49 dB respectively. The typical crosstalk is -35dB. Most parts of the DWDDM device are off-shelf optical components, ensuring that the cost is reasonable low. All the components were permanently fixed with Epoxy injection and UV-cured to make the device robust and rigid.

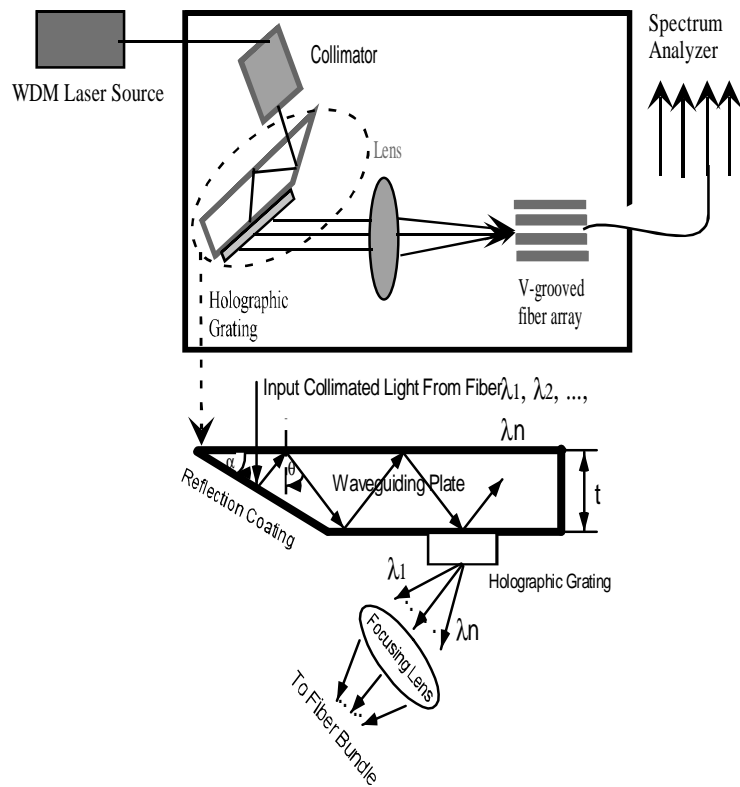


Fig. 3.1 Schematic of an eight-channel DWDM device, and the geometric structure of a path-reversed substrate-guided-wave interconnected model.

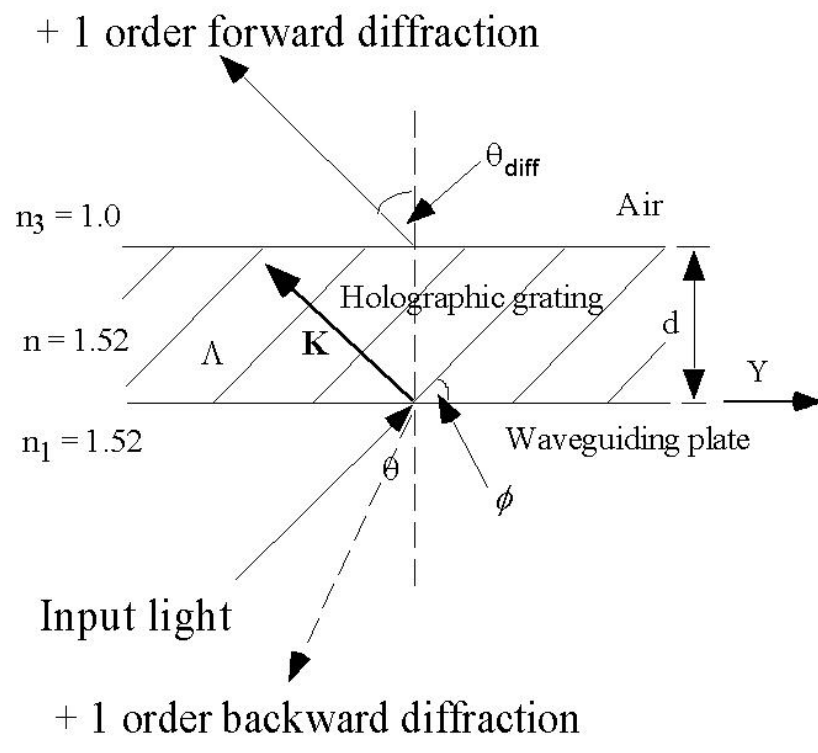


Fig. 3.2 Guided-wave holographic grating.

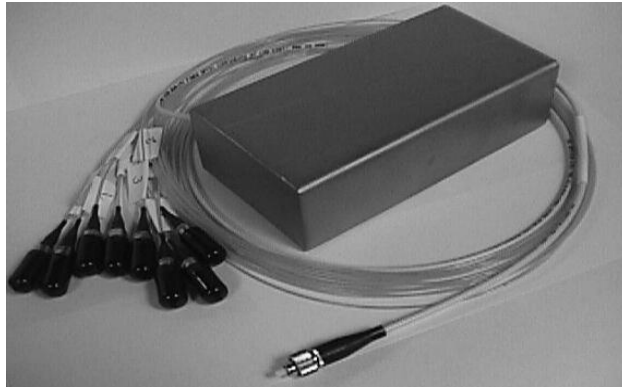


Fig. 3.3 (a)

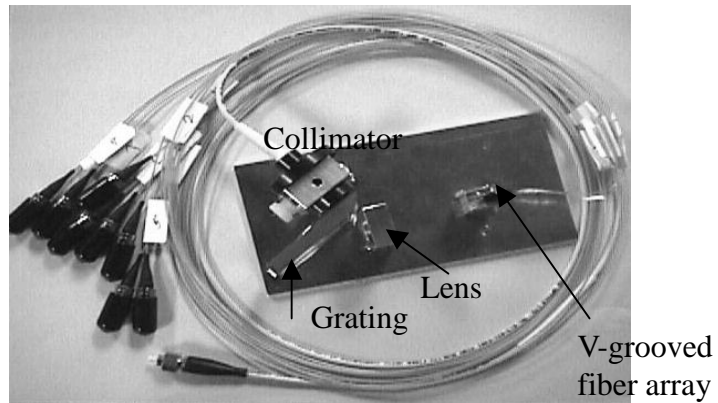


Fig. 3.3 (b)

Fig. 3.3 (a) Fully packaged eight-channel DWDDM device

(b) Inside setup of the packaged device

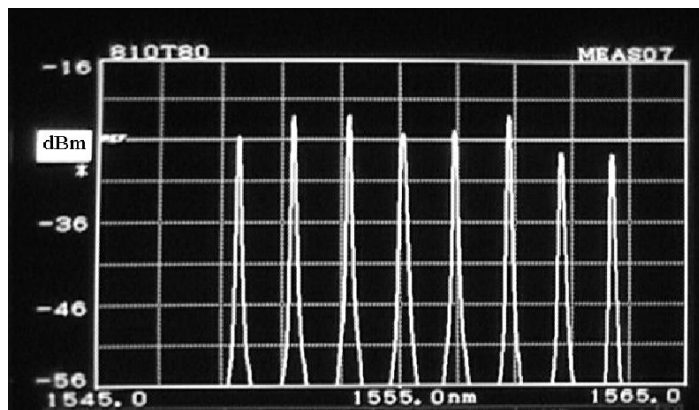


Fig 3.4: Output signals from an optical spectrum analyzer

Table 3.1 Spacing deviation for two different grating structures

Wavelength (nm)		1549	1551	1553	1555	1557	1559	1561	1563
Expected spacing to center wavelength (μm)		-750	-500	-250	0	250	500	750	1000
Spacing to center wavelength (μm) of two different structure	60°/60° structure	-725.92	-486.09	-244.15	0	246.43	495.24	746.52	1000.37
	60°/0° structure	-746.05	-497.36	-248.68	0	248.68	497.36	746.05	994.75
Deviations of spacing (μm)	60°/60° structure	-24.08	-13.91	-5.85	0	-3.57	-4.76	-3.48	0.37
	60°/0° structure	-3.94	-2.63	-1.32	0	-1.32	-2.63	-3.94	-5.25

Table 3.2 Insertion loss and crosstalk of the packaged device

Channel # &Wavelength (nm)	1	2	3	4	5	6	7	8
1. (1549.45)	-5.68	-5.72	- 40.80	-44.91	-45.82	/	/	/
2. (1551.37)	-3.12	-5.6	-36.3	-42.0	-46.6	/	/	/
3. (1553.20)	-42.2	-40.7	-5.40	-36.6	43.2	/	/	/
4. (1555.10)	-46.9	-42.9	-41.0	-5.3	-40.3	-43.27	-47.49	/
5. (1556.86)	/*	/	-41.7	-40.1	-5.68	-38.5	-46.1	/
6. (1558.79)	/	/	-41.9	-41.9	-38.3	-5.59	-40.1	-45
7. (1560.62)	/	/	-43.6	-43.5	-42.3	-33.5	-5.58	-39.2
8. (1562.65)	/	/	/	/	/	-39.9	-31.7	-5.49

Note: “*” means undetectable

Chapter 4: Athermalized Low-Loss Echelle Grating-Based Multimode Dense Wavelength Division Demultiplexer

Due to the explosive demand for high-bandwidth applications and the accompanying short distance, multimode dense wavelength division multiplexing has become an essential, robust, and high-performance data-link technology in metropolitan and local area networks (MANs and LANs) [70-76]. Multimode fiber represents the sizable portion of the fibers used in LANs, due to its low-cost installation and maintenance. It was being installed in LAN as early as the 1980s [77]. The WDM has been a cost-effective method of increasing the capacity of long-haul fiber links. But the WDM for data communications has to be quite low cost, compact, and compatible with multimode fiber. The potential for a large number of closely spaced channels and the inherent advantage of compactness make bulk diffraction grating-based demultiplexers quite attractive for multimode dense WDM applications [78-85]. Meanwhile, there is also an urgent need to find a way to overcome the temperature dependence in multimode DEMUXs, and to decrease the cost and the device size. In this chapter we present an athermalized low loss and low crosstalk DEMUX for MANs and LANs.

4.1 High-order echelle grating design principle and parameters

A high-order echelle grating has several special properties, which make it an excellent diffraction component for WDM diffraction. Most apparent is its high dispersion, which permits compact optical systems with a high throughput and high resolution. In addition, because it is never used far from the blaze direction, the grating efficiency remains relatively high over a large spectral range. Furthermore, when the grating is operated at higher orders, it is nearly free of the polarization effect [86]. Under the Littrow mount condition, when the incident angle is the same as the diffraction angle, another useful property comes into play: one lens can both collimate and focus simultaneously, resulting in lower cost and decreased packaging size for the WDM system. Figure 4.1 shows our measurements of the grating efficiency across all working wavelengths. The grating efficiency varies from 61%-75% within the whole working wavelength range (1549.32-1560.61 nm).

4.1.1 Calculation of desired diffraction order

Usually, the higher the grating order, the smaller the polarization effect of the grating. But any given grating order is also limited by certain factors. One of them is its working spectral range. We calculated the corresponding grating working order to cover the C band spectral range (from 1528 nm to 1560 nm). When the extremes of the C band are represented by $\lambda_1=1528$ nm and $\lambda_2=1560$ nm, the formula for calculating the grating order for a certain spectrum range can be expressed as [86]:

$$m = \frac{\lambda_1}{\lambda_2 - \lambda_1} \quad (4.1)$$

So that the spectrum of the C band signal λ_2 operating at m order does not overlap the spectrum of signal λ_1 when operating at $m+1$ order, m must be less than 47. On the other hand, we must leave room to fully reduce the noise caused by the scattering of adjacent orders.

We chose 22 as the grating working order, and the grating groove spacing ($18\mu\text{m}$) is large compared to the wavelength ($1.5\mu\text{m}$). This in turn implies that scalar theory of diffraction may be used. The scalar theory, based on the Huygens principle of secondary wavelets, assumes that the optical properties of the material of the grooves are the same on a microscopic scale as they are on a macroscopic scale. In other words, each groove facet is a small mirror or a small prism, but behaves in the same way as a large one. When the widths of the grooves are comparable with the wavelength of light this assumption is no longer valid.

For example, consider the operation of a metal mirror. The incident electromagnetic wave induces oscillations of the free conduction electrons in the surface of the metal. These behave as a series of oscillating dipoles, which re-radiate in phase with the incident wave and may be considered as a series of secondary sources, which interfere constructively in the direction of the reflected wave, in accordance with Huygens's theory. But when the dimensions of the facet are of the same order as the wavelength of the light, then the oscillations of the electrons are

impeded or curtailed by the boundary of the facet, and the simple scalar theory no longer applies. In practice when the groove spacing is less than about three times the wavelength, the efficiency curves for the two polarizations differ dramatically, and the “blaze wavelengths” differ [86]. By using 22nd-order grating, the diffraction efficiency is almost independent of the polarization of incident light.

4.1.2 Diffraction angle and angular dispersion calculation

In figure 4.2 the light is incident at angle θ_i and diffracted at an angle θ_d ; ϕ is the facet angle, where all three are measured from the grating normal. The reflection grating diffraction equation is [87]

$$n\Lambda(\sin\theta_i + \sin\theta_d) = m\lambda, \quad (4.2)$$

where m is the order of diffraction, λ the wavelength, Λ is the groove spacing, and n is the refraction index of the medium containing the incident and diffracted rays. Here, $n=1$. We found the angular dispersion by taking the first-order derivative of θ_d

$$\frac{d\theta_d}{d\lambda} = \frac{\sin\theta_i + \sin\theta_d}{\lambda \cos\theta_d}. \quad (4.3)$$

For the Littrow condition $\theta_i = \theta_d$, and angular dispersion is

$$\frac{d\theta_d}{d\lambda} = \frac{2 \tan\theta_d}{\lambda}. \quad (4.4)$$

The larger the diffraction angle, the greater the angular dispersion. In our design of the eight-channel DEMUX, the incident and diffraction angles are $\theta_i = \theta_d = 63.86^\circ$ at the center wavelength of 1555.32 nm, which is the 4th channel of our device. The

angular dispersion of the grating at the central wavelength ($\lambda=1555.32$ nm) was 2.62 mrad/nm.

Blazed grating redirects the incident light in the direction of a chosen diffracted order if each groove is formed appropriately. Thus in a transmission grating each groove constitutes a tiny prism, and for a reflection grating each groove consists of a small mirror inclined at an appropriate angle. The blaze condition is satisfied when the angle of incidence with respect to the facet normal is equal to the angle of reflection from the facet; *i.e.*

$$\theta_i - \phi = \theta_d + \phi; \quad (4.5)$$

$$\phi = \frac{\theta_i - \theta_d}{2} \quad \text{or} \quad \theta_d = \theta_i - 2\phi \quad (4.6)$$

Considering the Littrow mount, $\theta_i = -\theta_d$, so $\phi = \theta_d$, which is the situation depicted in figure 4.3. The grating blaze angle was 64° .

4.2 Device configuration and optical design details

The device was designed to have eight channel outputs and to be operated in the frequency region from 192.1THz to 193.5THz (Wavelength from 1548.90-1560.19 nm) within the ITU grid. The channel spacing is 200 GHz. Figure 4.4 shows a schematic diagram of this device. The input optical signals coming from a tunable external cavity semiconductor laser passed through 1-kilometer of coiled multimode fiber, which was used as a mode scrambler. The source was then introduced to the demultiplexer through the input channel of a silicon V-grooved multimode fiber

array. This 62.5/125 μm multimode fiber array has one input fiber and eight output fibers placed in single-layer silicon V-groove chip, which was designed to have variable fiber spacing because of the nonlinear effect of the angular dispersion. The channel spacing was 150, 151.57, 153.17, 154.88, 156.43, 158.29, 159.90 μm from the shorter wavelength to the longer wavelength end. An optimized diffraction limited triplet lens was used to collimate the incident light from the inputs and to focus the diffracted lights from the grating into the corresponding fiber array channels.

The grating used operates in a high diffraction order in order to minimize the polarization-dependent loss. The grating operates at large angles of incidence and diffraction in order to provide large angular dispersion. The large dispersion reduces the focal length of the lens, and hence the size of the instrument.

The 62.5 μm multimode fiber has a numerical aperture of 0.275, requiring the use of a lens large enough to accept and collect light with this numerical aperture across the entire fiber array. Figure 4.5 shows a cross section of the optics of the eight-channel demultiplexer. The vertical line at the left of this figure is the focal plane, and the front end of the fiber array (not shown) is in this plane. Light leaves the input fiber and is collimated by the lens. The grating gives an angular dispersion of the light into its constituent frequencies, the rays of one of which are shown in the diagram. The light for this frequency, 192.1THz, is focused by the lens onto an output fiber. For simplicity, rays for the other seven channels are not shown.

Because the size of the instrument is essentially proportional to the spacing of the fibers, which are only 150 μm in diameter, the fiber spacing could have been reduced to slightly less than this value, with a consequent reduction in size and weight of the device.

The lens is telecentric. That is, the input beam and all output beams are parallel to the optical axis. This fact has important consequences. First, insertion loss is minimized because all of the output beams are perpendicular to their respective fibers. Second, the frequency of a channel is invariant with respect to changes in focus. Since there are small changes in focus with changes in temperature, the frequency will not be a function of temperature. The experimental data below confirmed this fact.

The focal length f of the lens can be calculated by Equation 4.7 once the fiber spacing Δy and wavelength increment $\Delta\lambda$ between adjacent channels is known.

$$f = \frac{\Delta y}{\Delta\lambda} \frac{\lambda}{2 \tan \theta_d} \quad (4.7)$$

The above formula shows that the focal length of the lens is directly proportional to the fiber spacing and to the tangent of the angle of diffraction. Thus, in order to make the lens small, one can use closely spaced fibers and a large diffraction angle. For blazed grating, the diffraction angle is approximately equal to the blaze angle ϕ . For the center wavelength $\lambda=1555.32 \mu\text{m}$, $\Delta\lambda=1.6 \text{ nm}$, $\Delta y=154.88\mu\text{m}$, we can obtain $f=36.9\text{mm}$.

4.3 Simulation for the tolerance of image shift

Disturbances caused by laser drifting, temperature change, and vibration are reflected as a relative movement of the input light spot at the receiving fiber or as a shifting of wavelength. A larger 1-dB passband is therefore always preferable. To calculate the transverse loss of the WDM system, assume that the core diameter of the receiving fiber is $D=2R$, and the diameter of the input light spot is $d=2r$. We express the ratio of energy in the area of overlap (input light spot and receiving fiber) to energy in the entire area of the input light spot as

$$\eta = \frac{\int_{s'} f'(x, y) ds'}{\int_s f(x, y) ds}, \quad (4.8)$$

where η is the ratio of energy, s' is the overlap area, s is the input light spot area. The optical power distribution function at the overlap area and the whole area of input light spot are $f'(x, y)$, $f(x, y)$ respectively. Figure 4.6 illustrates Equation 4.8. We can obtain the maximum tolerance of image shift when the WDM system functions within 1-dB passband range.

Here, we assume a uniform power distribution across the whole area of the input light spot. We simulated the theoretical 1-dB passband calculation, in which $D=62.5\mu\text{m}$ and $d = 62.5\mu\text{m}$. Figure 4.7 shows the simulation result, which indicates that when a system is diffraction-limited, *i.e.*, the input spot size is the same as the multi-mode fiber core diameter; the maximum image shift tolerance can be up to $\pm 10\mu\text{m}$

within 1dB passband. This large image shift tolerance helps the device to resist various kinds of environmental disturbances.

4.4. High data transmission bit rate

To achieve a high data transmitting bit rate in the telecommunications field is the goal of WDM technology. The maximum bit rates are determined by numerous factors, including the signal modulation rate, the transmission bandwidth through the transmission media, and the response time of the opto-electronic devices. In a communications network, the WDM system is simply one part of the transmission regime. The pulse broadening of grating-based DWDM imposes inherent limitations on the data transmission bit rate. We need to optimize the WDM design to decrease pulse broadening caused by grating, which can be calculated by the formula below:

$$\Delta\tau_g = \frac{n_0 \cdot f \cdot \tan(NA) \cdot \tan(\theta_d)}{2c} \quad (4.9)$$

where, the intensity of input light posses Gaussian distribution; n_0 is the refractive index of the media where light is transmitted, c is the speed of light at vacuum. $NA=0.275$, is the numerical aperture of the input fiber. The focal length of the lens $f=36.9\text{mm}$. $\theta_d = 63.86$ is the diffraction angle of grating. So, the pulse broadening caused by grating is $\Delta\tau_g=3.4 \times 10^{-11}\text{s}$. Equations 4.9 clearly shows that, when working at a certain wavelength, pulse broadening caused by gratings is proportional to the numerical aperture of the input fiber, to the focal length of the lens, and to the diffraction angle of the grating.

Mode dispersion is another major factor causing pulse broadening in multimode DWDM. For graded index multimode fibers, the pulse broadening can be calculated by Eq. (4.10)

$$\Delta\tau_m = \frac{Ln_1}{8c}\Delta^2 \quad (4.10)$$

Where, the refractive index of the core is $n_1=1.473$; relative index difference is $\Delta=1.74\%$; the speed of light in the vacuum $c=3\times 10^8$ m/s; $L=100$ m is the length of the multimode fiber. The calculated pulse broadening caused by mode dispersion $\Delta\tau_m=1.9\times 10^{-11}$ s. The total pulse broadening can be calculated by Eq. (4.11)

$$\Delta\tau = \sqrt{\Delta\tau_g^2 + \Delta\tau_m^2} \quad (4.11)$$

The maximum data transmission bit rate can be expressed as Equation (4.12) when neglecting initial pulse width.

$$BR = \frac{1}{4\Delta\tau} \quad (4.12)$$

Here, the total pulse broadening $\Delta\tau=4.3\times 10^{-11}$ s, therefore the theoretical bit rate $BR = 5.8$ Gbps. We measured the data transmission bit rate using the setup shown in Figure 4.8. The maximum signal speed of the signal generator was 3.5 Gbps. The random signal from the signal generator at the speed of 3.5 Gbps was sent to a modulator to modulate the intensity of the optical signal from a tunable laser. The modulated optical signal passed through a mode scrambler and then was sent to the input channel of the WDM device. A digital communication analyzer was used to measure the eye diagram of the output channels. Figure 4.9 shows a clearly open eye diagram when

the input optical signal was modulated at 3.5Gbps. The applied current is 120 mA; the ratio of signal to noise is $S/N=8.7$.

4.5 Device performance

The multiplexer was fabricated as a stand-alone unit deploying a stainless steel housing to provide compatible thermal expansion coefficient with the lens material. The entire assembling and packaging process is passive and epoxy-free, which avoided the possible wavelength and insertion loss shifting caused by the UV curing of epoxy. Figure 4.10 shows the inside of the fully packaged 8-channel multimode demultiplexer. By improving the mechanical design, by careful choices of optical materials, by employing the epoxy-free packaging and sealed package housing, we have obtained excellent thermal behavior for this DEMUX, from the point view of insertion loss, as well as center wavelength accuracy. The detailed thermal analyses will be given in Chapter 5.

We measured the transmission spectrum using an amplified spontaneous light emission (ASE) light source and an optical spectrum analyzer having a 0.01 nm resolution. All the measurement results were obtained after taking the average of three sets of the input and output signals. Figure 4.11 shows the transmission spectrum for each of the eight channels. These figures were measured at the wavelength of minimum loss, which was always within 0.04 nm of the nominal channel center wavelength. The lowest insertion loss for any channel was 1.50 dB; all of the channels show under 2.70dB loss with a mean figure of 1.95dB, which includes

connector loss. Of the 1.95 dB, 1.55dB is due to the grating diffracting 70% of incident power into the desired diffraction order. 0.1dB is caused by lens transmission and reflection loss; and the other 0.3dB is caused by fiber array coupling and connection loss.

We also monitored the change in insertion loss and center wavelength when increasing the operating temperature from 20°C to 60 °C. The average insertion loss changed from 1.95dB to 2.34dB, which gave a 0.00975dB/degree loss shift. Figure 4.12 shows the loss variation against different channels at 20°C and 60°C. We could then find that the maximum change of the 8 channels in loss was 1.1dB, which was within the loss deviation range of 1.2dB for different channel at room temperature. The average wavelength shift with temperature is 0.00033 nm/°C.

The wavelength temperature dependence was successfully suppressed within 0.032 nm in the 20 to 60°C temperature ranges, which is also within the wavelength accuracy range at room temperature. The detailed measured device parameters are listed in Table 4.1. The wavelength accuracy is within 0.04 nm in the worst case, which was due to the imperfect positions of fibers in the array and the output power shifting of the white band ASE light source. The device has fairly good isolation; the average crosstalk is 46.5dB. The measured 1dB and 3dB bandwidths are 0.34, 0.60 nm respectively. The typical polarization dependence loss was measured to be 0.13dB.

4.6 Summary of Chapter 4

We designed and demonstrated a high resolution and low insertion loss athermalized grating-based 8-channel DEMUX. This device has 1.95 and 2.34dB insertion loss at 20°C and 60°C respectively. The mean crosstalk is 46.7dB. To the author's knowledge, those are the best-reported results for a multimode DWDM. The wavelength accuracy is within 0.04 nm. The 3dB passband was measured to be 0.60 nm. This low-cost and highly stable DEMUX can be employed for both metropolitan and local area networks.

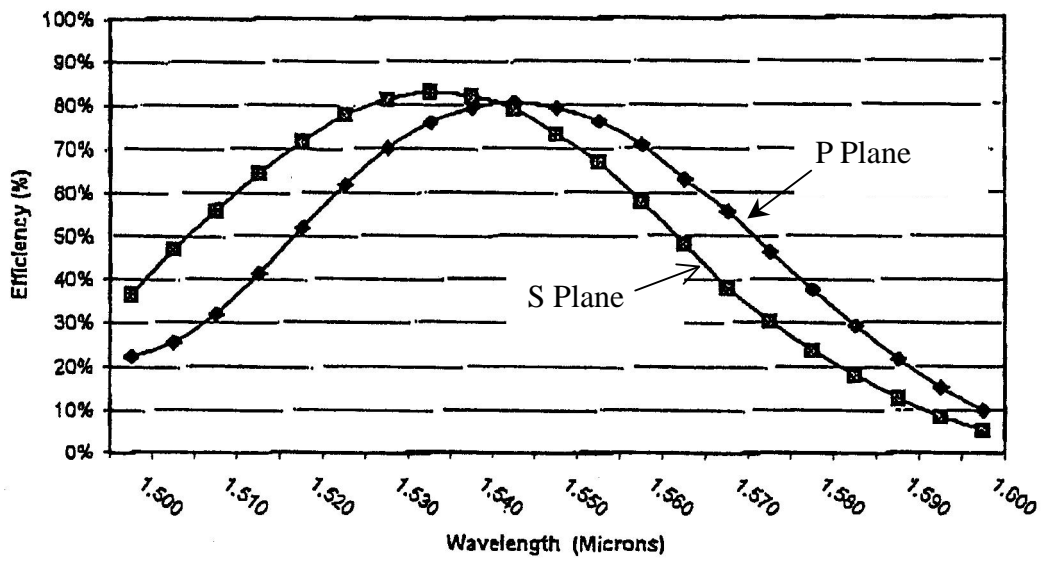


Fig. 4.1 Diffraction efficiency of the 22nd echelle grating

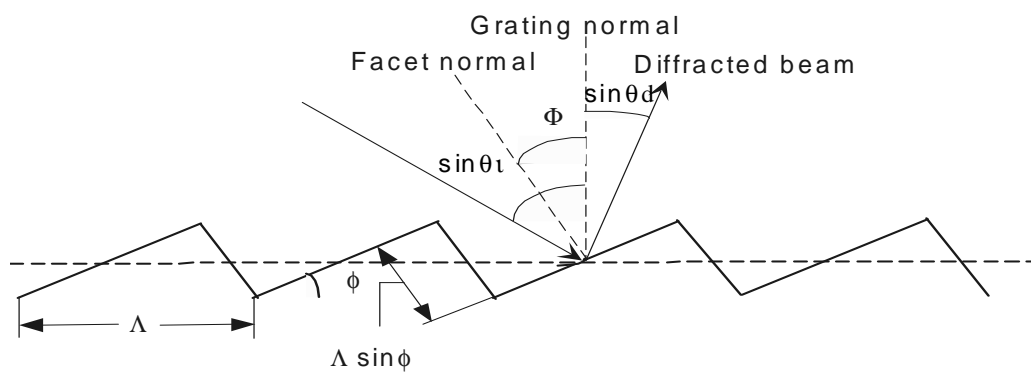


Fig. 4.2 Configuration of a blazed grating

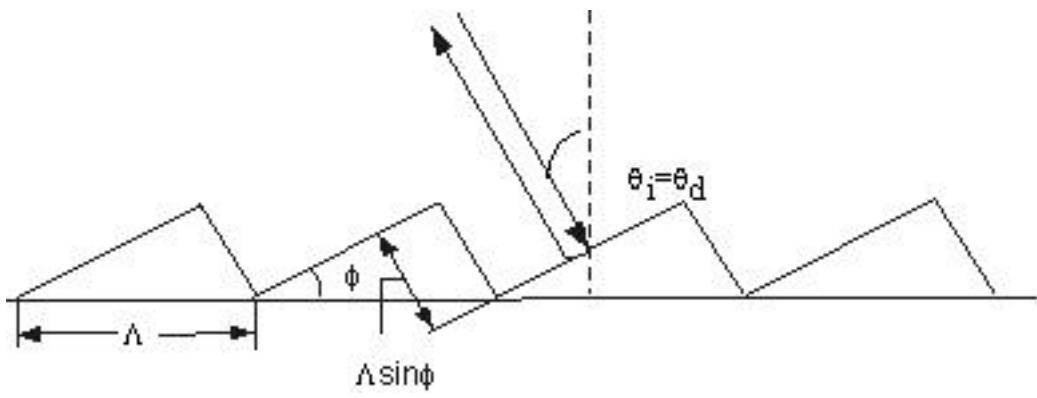


Fig.4.3 A blazed grating used in the Littrow mounting

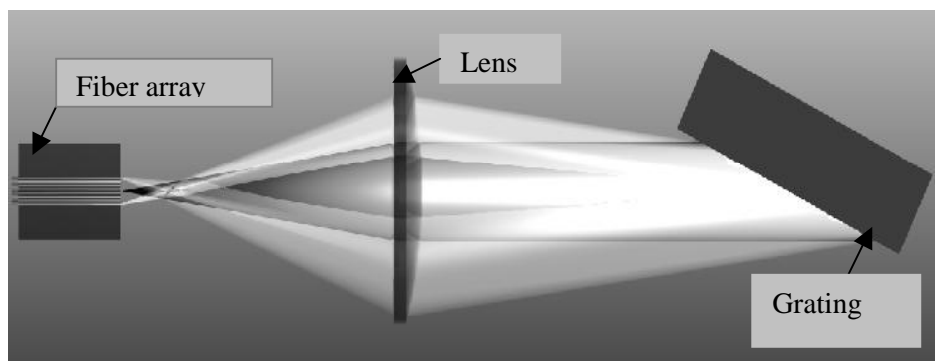


Fig.4.4 Geometrical layout of the eight-channel multimode demultiplexer

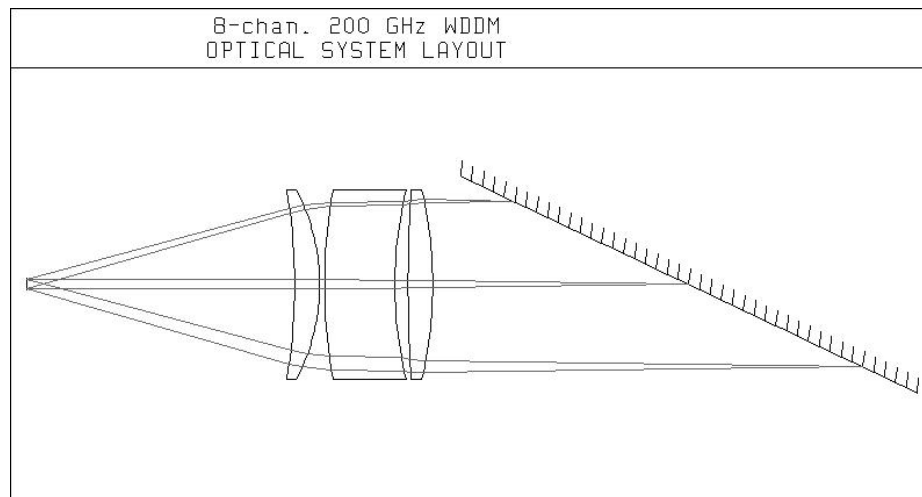


Fig. 4.5. A cross section of the optics of the eight-channel demultiplexer

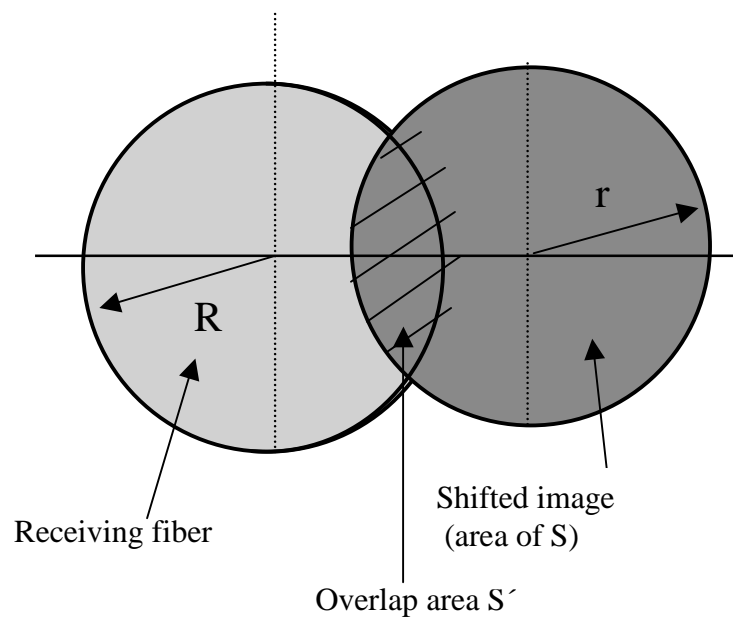


Fig. 4.6. Illustration of the overlap region of a receiving fiber and the input spot

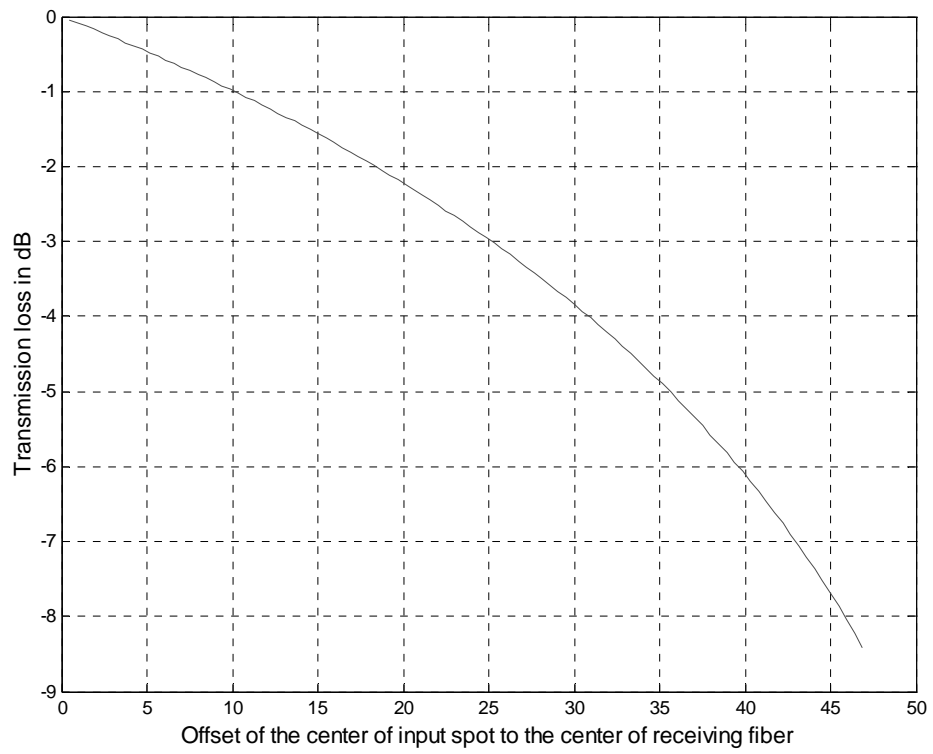


Fig. 4.7 Simulation result shows $\pm 10\mu\text{m}$ image shift tolerance within 1dB passband.

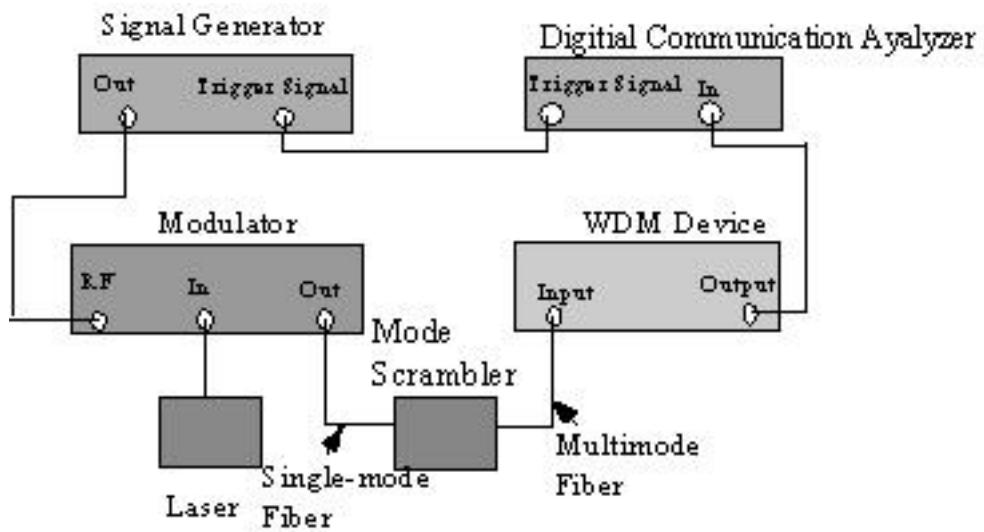


Fig. 4.8 Experimental setup for data transmission bit rate testing

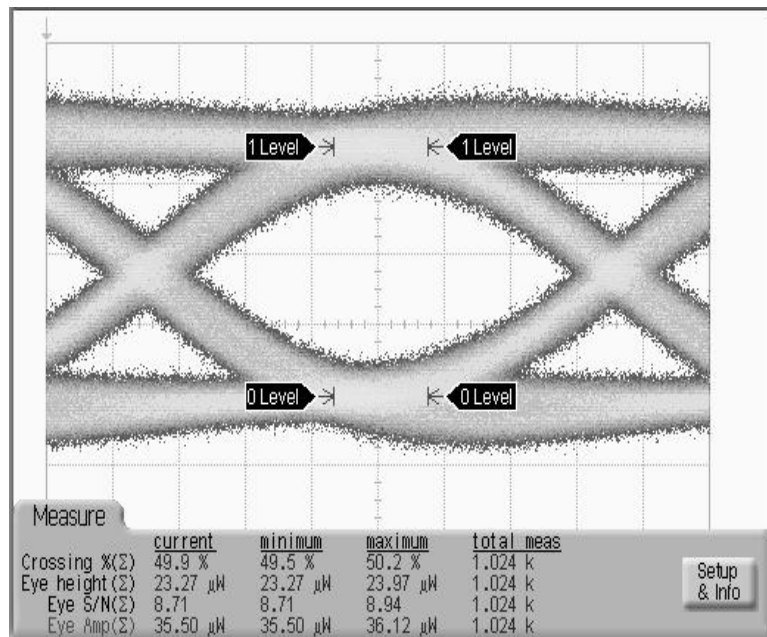


Fig. 4.9 Experiment confirms that the data-transmission bit rate of the demultiplexer is higher than 3.5 Gbps.

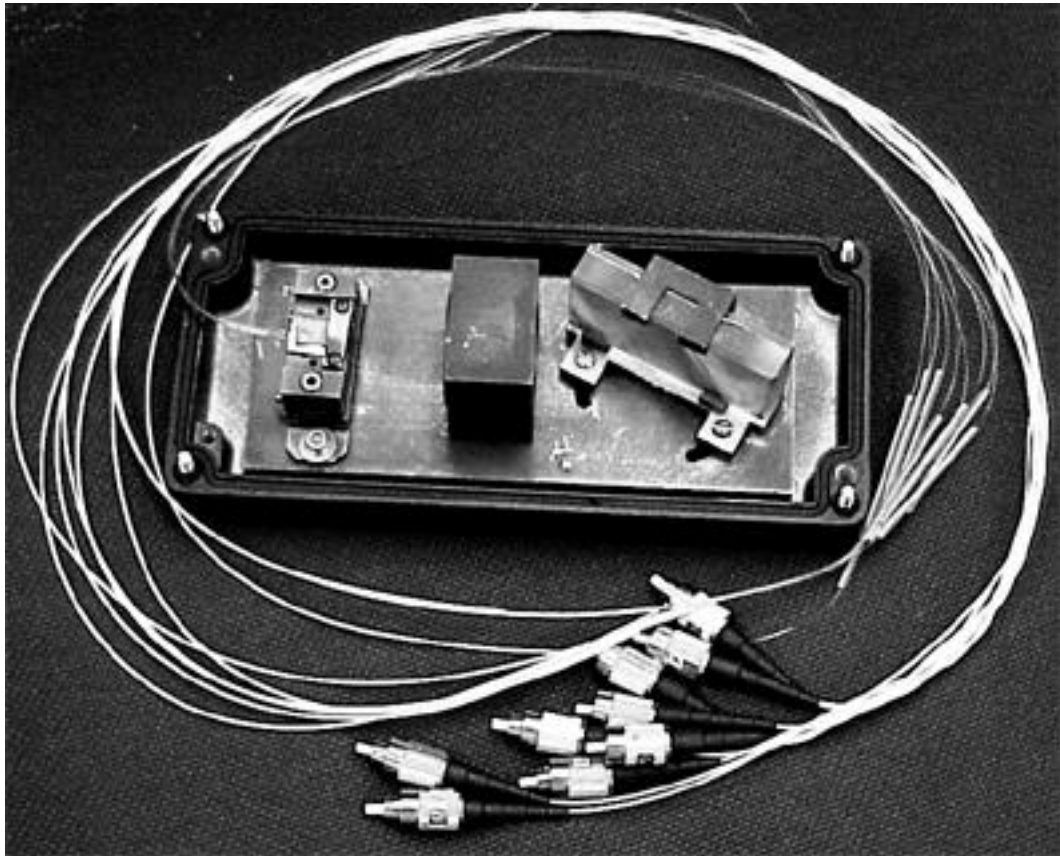


Fig. 4.10 Inside of the fully packaged eight-channel multimode-in, multimode-out demultiplexer.

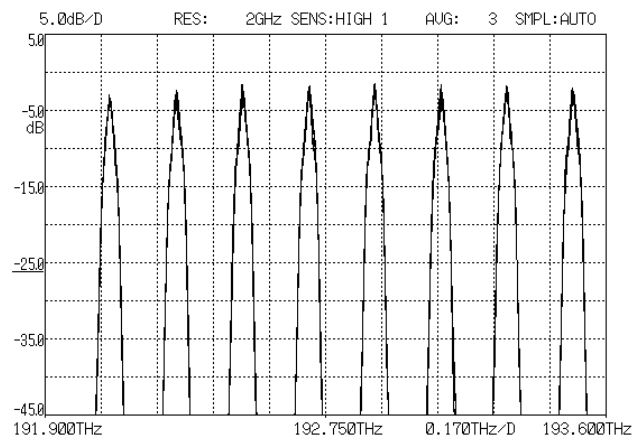


Fig.4.11 Output spectrum of the demultiplexer. The resolution of the optical spectrum analyzer is 0.01nm. The result was obtained by taking the average of three sets of measurement.

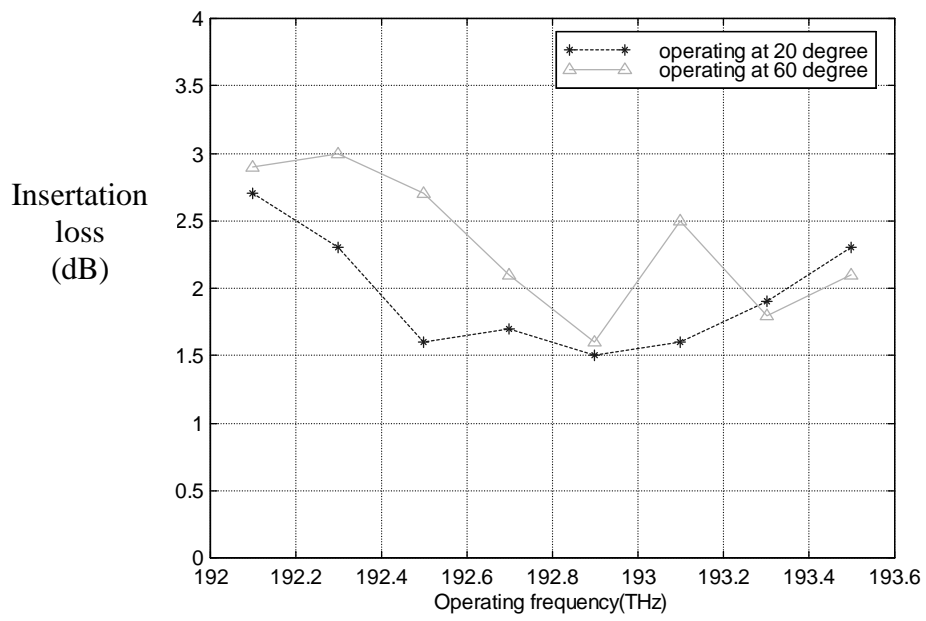


Fig. 4.12 Insertion loss variation plotted against channel frequency at 20°C and 60°C

Table 4.1 Device parameters of the multimode demultiplexer.

	Ch#1	Ch# 2	Ch# 3	Ch# 4	Ch# 5	Ch# 6	Ch# 7	Ch#8
Designed Center	1560.61	1558.98	1557.36	1555.75	1554.13	1552.52	1550.92	1549.32
wav. (nm)								
Waveleng. Error at 20°C (nm)	0.02	0.02	0.04	0	0.02	0.01	0	0.02
Waveleng. Error at 60°C (nm)	0.02	0.04	0.008	0.008	0.016	0.032	0.032	0.024
Insertion loss (db)	2.7	2.3	1.6	1.7	1.5	1.6	1.9	2.3
CrossTalk (db)	47.8	47.6	48	48	46	45.7	44.6	44.4
3dB BW (nm)	0.6	0.61	0.6	0.6	0.6	0.6	0.56	0.6
PDL(dB)	0.2	0.15	0.07	0.1	0.28	0	0.16	0.07

Chapter 5: Thermal Analysis and Compensation of Grating-Based Wavelength Division Demultiplexers

When temperature changes, insertion loss and center wavelength may change accordingly. The center wavelength shift is mainly caused by the change in grating groove spacing and the change of fiber position along the dispersion direction. The change in insertion loss is due to the thermal variation in lens focal length, and the image shift in vertical and horizontal direction caused by the difference in the thermal coefficient of expansion (TCE) of lens and its supporting material. It is desirable to design wavelength division demultiplexers (WDDMs) in such a way as to eliminate or reduce changes in performance that are caused by temperature fluctuations.

A typical operating temperature range is -5°C to 60°C , so we were seeking nearly constant performance over this range. We will show in this section that it is possible to eliminate or reduce the thermal effect by careful optical design and by judicious choices in constructing the grating, lens, and housing.

5.1 Effects caused by the various parts

A vertical cross section of a typical WDDM of our design is shown in Figure 5.1. For ease of interpretation, the tilt of the grating is omitted. From the figure, in the latter drawing the fibers are not shown, the simplified lens is replaced by an actual lens, and the grating is shown as a flat, shaded, tilted plane.

Thermal compensation may be achieved by dividing the problem into three parts. *First*, we show that thermal changes in grating dispersion occur unless the grating material has a zero coefficient of expansion. Thus, we use zero-expansion gratings in most of our WDDMs.

Lens materials are more complex than grating materials in that they possess both a coefficient of thermal expansion and a temperature derivative of the refractive index. Thus one cannot merely use zero-expansion lens materials unless these materials also have refractive indices that are invariant with temperature. We are not aware of any materials that meet both of these criteria, except for mirrors. The *second* part of the problem calls for keeping the fibers in focus as the temperature varies, as well as keeping the thermal variation in lens focal length small enough to be negligible.

The *third* part of the problem involves shifts of the optics in the vertical direction. Referring to Figure 5.1, this is the x -direction. The lens assembly is symmetric about the x - z plane, and the fiber assembly is nearly symmetric about this plane, so that there will be no shifts in these components in the y -direction. The front surface of the grating will, in general, move along both the y and z axes due to expansion of its backing plate (see Figure 5.1). However, since the grating is used in collimated light, this movement will have no effect other than a minute lateral shift of the collimated beam. This shift can readily be shown to be a negligible fraction of the size of the clear aperture of the lens, and will therefore have a negligible effect on the performance, or no effect at all if the beam is smaller than the lens aperture (the usual

case). In summary, there are only three effects of importance, enumerated above. We discuss these effects in detail in the following sections.

5.2. Center wavelength shift

5.2.1 Effect of grating thermal expansion

We consider here a WDDM that is designed as a Littrow spectrograph, as shown in Figure 5.2. The lens collimates the light from the input fiber and sends it to the grating. The grating separates the light into its constituent wavelengths and sends the angularly dispersed spectrum to the lens. The lens focuses the linearly dispersed spectrum onto the focal plane, and each output fiber receives a different portion of the spectrum. Typically, the spectral range is less than 5% of the central wavelength, so that the wavelength is, to a first approximation, constant.

Let Λ represent the grating groove period, θ_i, θ_d the angles of incidence and diffraction, m the grating working order, and λ the working wavelength.

The grating equation can be expressed as

$$\Lambda(\sin\theta_i + \sin\theta_d) = m\lambda. \quad (5.1)$$

We define the grating's linear temperature coefficient of expansion (TCE) as:

$$\Lambda = \Lambda_0(1 + \beta \cdot \Delta T), \quad (5.2)$$

where β is the TCE of the grating, and ΔT is the change of temperature. Assuming that the incident and diffraction angle remain constant with temperature, we can easily find the wavelength shift with temperature change thus:

$$\Delta\lambda = \beta \cdot \lambda \cdot \Delta T \quad (5.3)$$

Replica gratings have a substrate that is coated with a thin layer of epoxy, which forms the surface-relief features of the grating. The epoxy in turn is coated with a quite thin layer of metal to give the finished grating reflecting properties. We assume that the expansion of the grooves is equal to the expansion of the substrate, because the substrate is much thicker than its coatings. When temperature changes within a certain range, the larger the TCE of the grating substrate, the greater the shift in center wavelength. We substitute typical values into Eq. (5.3), as follows. Let $\lambda_0 = 1555$ nm, $T_0 = 20$ °C, $T = 60$ °C, and use BK7 glass. The expansion coefficient of this glass is $7.1 \times 10^{-6}/\text{K}$ [88]. From (5.3), we have $\Delta\lambda = 0.44$ nm. Suppose the channel bandwidth $\Delta\lambda'$ is 0.4 nm, which is a typical 3-dB width for a WDDM with narrow channel spacing. Then $\Delta\lambda = 1.1\Delta\lambda'$, which represents an extremely large effect. Now suppose that $\Delta\lambda' = 11$ nm, such as is typical for wide channel spacing. Then $\Delta\lambda = 0.036\Delta\lambda'$, and the effect on performance will be negligible.

The grating we deployed for the DWDM has ultra-low TCE. The TCE is zero from 0-35°C, and less than $0.06 \times 10^{-6}/\text{°C}$ when the temperature is higher than 35°C (which is 1180 times less than the TCE of BK7). When operating at the same wavelength and temperature range, Eq. (5.3) predicted a maximum $\Delta\lambda = 0.037$ nm wavelength shift which was in good agreement with the experimental result $\Delta\lambda = 0.032$ nm showed in Section 4.5. Deploying ultra-low expansion grating suppressed the wavelength shift successfully.

Our conclusions were twofold. First, the center wavelengths of all channels will shift with temperature by an amount $\Delta\lambda$ that is nearly the same for all channels, due to the fact that the spectral range is small compared to the mean wavelength. Second, when designing a WDDM that has channel bandwidths that are on the order of 0.0071 times the wavelength (a so-called coarse WDDM), one can use optical glass for the grating substrate material. For narrower bandwidths, the thermal shifts of glass gratings become very significant, and one must either resort to the use of low-expansion grating materials or compensate for thermally induced changes in the grating period. We have chosen to use low-expansion materials, since they simplify the design and eliminate residual variations in $\Delta\lambda$.

5.2.2 Effect of fiber mount in direction of dispersion

We found the amount $\Delta y_{fm,n}$ by which the n th fiber moves away from the optical axis when the temperature is raised from room temperature, T_0 , to the maximum operating temperature, T_1 . This parameter originates from thermal expansion of the fiber mount, hence the subscript “fm.” Using this data and the known linear dispersion of the instrument $\partial\lambda/\partial y$ at wavelength λ , we can predict the change in wavelength due to fiber mount expansion $\Delta\lambda_{fm,n}$ by the equation

$$\Delta\lambda_{fm,n} = \Delta y_{fm,n} \frac{\partial\lambda}{\partial y}. \quad (5.4)$$

The equation for the linear expansion of a material as a function of temperature is

$$L_1 = L_0[1 + \alpha(T_1 - T_0)], \quad (5.5)$$

where L_0 is the length of the material at temperature T_0 , L_1 is the length of the material at temperature T_1 , and α is the coefficient of the material's linear expansion. In the eight-channel 200 GHz units described in the previous chapter, the fiber mount was made out of silicon, which has a coefficient of expansion of 2.33×10^{-6} per centigrade degree. These units have a nominal fiber spacing of 150 μm ; the distance y_{end} of the endmost fiber from the optical axis is 0.60 mm; and the linear dispersion is about 0.00649 nm per micrometer. Let $T_0 = 20^\circ \text{C}$ and let $T_1 = 60^\circ \text{C}$; then $\Delta y_{fm,end} = L_1 - L_0 = +5.59 \times 10^{-5} \text{ mm}$.

By combining Eqs. (5.4) and (5.5), we found that $\Delta\lambda_{fm,end} = +0.000363 \text{ nm}$.

This is a negligible change in wavelength.

In conclusion, for eight-channel devices with channel spacing of 150 μm or less, our analysis has shown that the change in wavelength of any channel due to lateral expansion of the fiber mount is quite small. Such effects will be negligible for fiber mounts composed of metal, ceramic, or silicon. However, the lateral expansion of the fiber mount plays a more significant role as the number of channels increases. For devices with more than eight channels or with fiber spacing greater than 150 μm , one must calculate the effect of lateral expansion upon the channel center wavelengths and, if necessary, compensate for it.

5.3 Image shift caused by thermal effect

5.3.1 Effects in the vertical direction

The vertical direction is the x - z plane, as shown in Figure 5.1. Our first observation concerns the grating. Since the grating has no optical power in the vertical (x) direction, its vertical expansion has no effect.

In our WDDMs (see Fig. 5.1) all parts that support the optics, except the V-groove (*i.e.*, the fiber holder), are made of the same material. Let this material have a linear coefficient of expansion α_M . The V-groove, which holds the fibers, is quite thin, and no fiber is ever more than 1.64 mm above a thin layer of cement (not shown) that holds the V-groove to the pedestal. At present, the V-groove is silicon, which has a coefficient of expansion of 2.33×10^{-6} per $^{\circ}\text{C}$. A typical operating temperature range is 20 to $+60$ $^{\circ}\text{C}$. According to Eq. (5.2), the 1.64 mm dimension changes to 1.64025 mm, as the temperature is increased from 20 $^{\circ}\text{C}$ to 60 $^{\circ}\text{C}$. The change in fiber location is only 0.25 μm , which is negligible compared to 62.5 μm , the diameter of a typical output fiber. We thus disregard the thickness of the V-groove. If the cement thickness is 0.5 mm or more, its expansion will have a noticeable effect, since cements typically have expansion coefficients of $\sim 50 \times 10^{-6}$ per degree C. The thickness of cement can be easily controlled within 0.025mm, so we neglect this effect in what follows. Especially, for single-mode DWDM design, we eliminate the usage of cement to minimize the image shift in vertical direction.

We make the assumption that the lens remains in contact with the *lower* part of the lens cell as the temperature changes. The validity of this assumption depends upon the precise means by which the lens is held in its cell, and different methods of mounting will dramatically change the results of our analysis. For instance, if the lens remains in contact with the upper portion of the lens cell, the sign of the result [Eq. (5.10)] is reversed.

The system is initially aligned at room temperature T_0 . At this temperature the fibers and the center of the lens are both at a height H above the baseplate. At a new temperature, T_1 , the fiber height is

$$x_F = H(1 + \beta_M \Delta T), \quad (5.6)$$

where $\Delta T = T_1 - T_0$. At temperature T_1 , the center of the lens is at a height of

$$x_L = (H - \frac{1}{2}D)(1 + \beta_M \Delta T) + \frac{1}{2}D(1 + \beta_L \Delta T), \quad (5.7)$$

where β_L is the coefficient of expansion of the lens. D is the diameter of lens. At this temperature, the fiber height exceeds the lens center height by the distance

$$\Delta x = x_L - x_F = \frac{1}{2}D\Delta T(\beta_L - \beta_M). \quad (5.8)$$

Because the lateral magnification of the system is -1 , the image of the fibers also moves by the distance $-\Delta x$ relative to the center of the lens. Thus, the image of the fibers has moved away from the fibers themselves by a distance of $-2\Delta x$, and the vertical distance between the image and the fibers is

$$-2\Delta x = -D\Delta T(\alpha_L - \alpha_M). \quad (5.9)$$

Letting x_I be the distance of the image from the baseplate, Eq. (5.9) becomes

$$x_I - x_F = -D\Delta T(\alpha_L - \alpha_M). \quad (5.10)$$

We call the quantity $x_I - x_F$ the image shift. Equations (5.9) and (5.10) give the distance between the image of the fibers and the fibers themselves in terms of the lens diameter, the temperature change, and the coefficients of expansion of the lens and of the supports. We have assumed that all supports are made of the same material.

Equation (5.10) indicates that, when the temperature changes within a certain degree, the better matched the TCE of the lens and its supporting materials, the less the image shift, and then the less the insertion loss shift. The differential expansion in the vertical direction is directly proportional to the lens diameter, so that thermal problems become severe for large lenses unless the expansion coefficients of the lens elements are nearly equal to each other and to that of the support. For the eight-channel dense multi-mode WDDM ($D=39.6\text{mm}$), we used stainless steel as supporting material for all the parts whose TCE is $9.9\times 10^{-6}/\text{K}$. We chose F7 as lens material since it has almost the same TCE ($9.8\times 10^{-6}/\text{K}$) as stainless steel. Its image shift is $0.16\ \mu\text{m}$, which can be ignored compared to the fiber core diameter.

5.3.2 Effect in the lateral direction

Because the WDM system is symmetric in the lateral direction, the image shift in the lateral direction is mainly caused by the change of central wavelength. The image shift Δy corresponding to the original designed position can be expressed as

$$\Delta y \cong \frac{2 \cdot \Delta \lambda \cdot \tan \theta_{diff} \cdot f}{\lambda} \quad (5.11)$$

where θ_{diff} is the diffraction angle at a working wavelength λ ; $\Delta \lambda$ is the shift of working wavelength caused by temperature variation. The focal length is f . Combining equations (5.3) and (5.11), We can easily obtain the relation between the lateral shift and the TCE of grating material and temperature change.

$$\Delta y \cong 2\beta \cdot \Delta T \cdot f \cdot \tan \theta_{diff} \quad (5.12)$$

It is obvious that the larger the diffraction angle, or the larger the TCE of the grating material, the greater the lateral image shift with temperature. In our design, the lateral image shift is effectively suppressed to be less than $0.058\mu\text{m}$. The insertion loss caused by image shift in either direction is insignificant, considering the large core size of the multimode fiber. The conclusions obtained in this section were based on the assumption that the alignment is perfect. A WDDM can give excellent performance at room temperature, but still be misaligned. This misalignment can cause significant changes in signal as the temperature changes. Thus, it may be necessary to check that, at room temperature, an alignment parameter is near the center of its range, not merely within its range.

5.4. Change in lens focus

We analyzed the thermal performance of the lens shown in Figure 5.1 and found that its focus relative to the end of the fiber mount varied with temperature. Referring to Figure 5.3, the change in back focal length Δf_b due to a change in temperature ΔT must be equal and opposite to the change in length Δz_m of the portion of the baseplate that lies between the lens and the fiber mount. That is,

$$\Delta f_b = -\Delta z_m. \quad (5.13)$$

In order to correctly calculate thermal changes in the WDDM, one must consider thermal changes in the refractive index of each lens element, the thermal expansion of the lens elements, the thermal expansion of the spacers between the optical parts, and the thermal expansion of the grating period. All of these parameters were handled by the optical design software (ZEMAX) that we used, so that we were able to accurately simulate thermal changes of back focal length and overall optical performance.

Because available optical glasses have wide variations in the first derivative of the refractive index with respect to temperature, one is able to select a glass or glasses for the lens elements that not only will satisfy Eq. (5.13) for a chosen baseplate material, but will also provide an opportunity for the lens to be aberration-corrected over the entire temperature range. That is, we have been able to fully optimize our lenses to have athermal performance, considering the effect of expansion in the lens spacers and the mount. This is a considerable improvement, compared to the

conventional approach of merely keeping the effective focal length or the back focal length constant.

For example, the WDDM in Chapter 5 has a 0.275 NA, and 150 μm fiber spacing. We used F7 as lens material, in conjunction with Type 416 stainless steel mounts and lens spacers, and produced optical performance that was diffraction-limited at all wavelengths and invariant with temperature. We expect this design to have no observable changes in insertion loss with temperature, provided the alignment is perfect, and the fiber array is mounted in such a way that the fiber ends remain above the same point on the base plate at all temperatures. This can be done by clamping the fiber array at the end nearest the lens and letting the other end change its position with temperature. Other means of achieving this effect while having both ends clamped are possible, but are not discussed here. Section 4.5 shows a maximum 1.1dB of insertion loss shift across temperature operation range 20-60°C. This insertion loss shift was mainly due to that the alignment was not perfect.

Equation (5.13) does not guarantee that the focal length of the lens will be invariant with temperature, only that the lens will stay in focus. The focal length and back focal length are strongly correlated, but not identically so. The focal length can be controlled by thermal optimization of the lens design.

5.5 Chapter 5 Summary

In Chapter 5, we analyzed the thermal effects on diffraction grating based DWDMs. When the temperature changes, normally the various parts of the DWDM will expand with rising temperatures and shrink with falling temperatures. Various responses from different parts of the device upon central wavelength accuracy and insertion loss were discussed. Central wavelength shift is mainly caused by the effect of the grating's thermal expansion. Insertion loss shift is mainly due to the change of focal length and image shift in both the vertical and horizontal directions. By adopting the ultra-low expansion gratings; compatible materials for lenses, spacers, holders, housings; and optimized optical design, it is possible to build thermal-insensitive WDM devices.

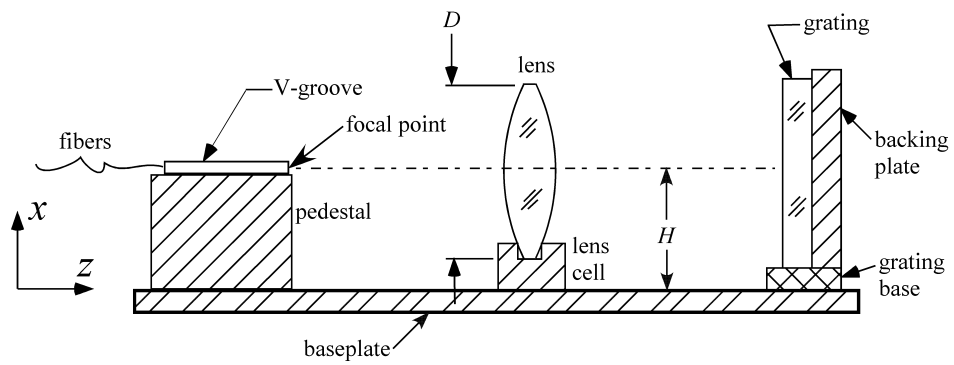


Fig. 5.1. A simplified cross sectional view of a typical echelle grating based WDDM. The dispersion is in the y - z direction, and the y -axis points away from the reader's eyes.

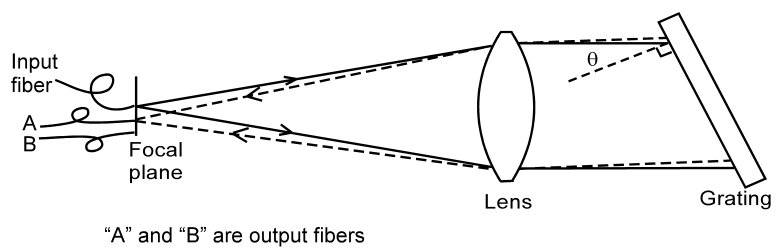


Fig. 5. 2 WDDM in Littrow mount

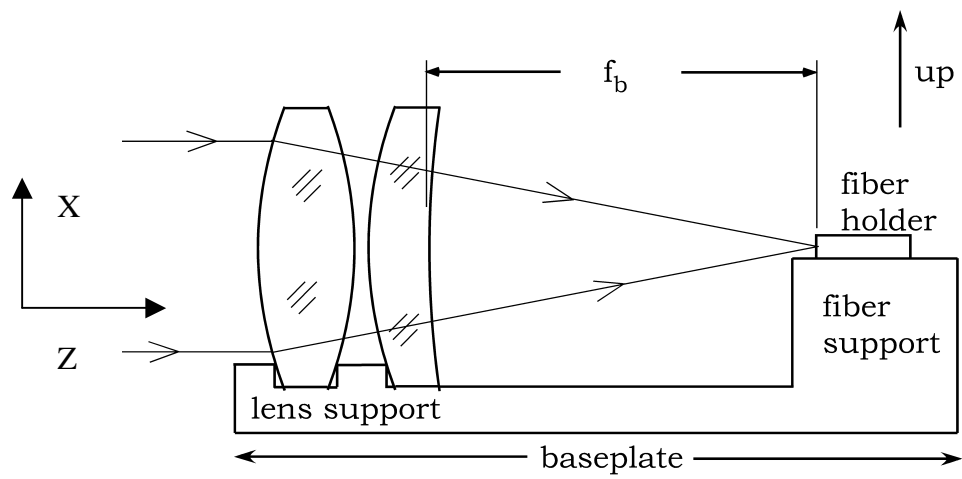


Fig. 5.3. A simplified cross-sectional view of the section of a WDDM that includes the lens and the fiber holder.

Chapter 6: 32-Channel 100-GHz Echelle Grating-based Demultiplexers

Rapid growth in the demand for high-capacity telecommunications links, in the context of the speed limitation of single-wavelength links, has generated worldwide interest in dense wavelength division demultiplexers (DEMUXs) [29-33,89] as an effective higher-capacity solution for optical networks. Several major technologies for making DEMUXs include interference filters, Bragg grating filters [16-21], and phased-array-based DEMUXs [22-28]. Technologies using interference filters and Bragg grating filters experience a low level of fiber-to-fiber loss, but the losses are not uniform across the whole wavelength range. Interference filters and Bragg grating filters use discrete components, so that increasing the number of channels proportionately increases the cost as well as the volume of packaging. Interference filters entail multi-cavity structures requiring tens of tightly controlled dielectric layers in order to produce individual filters. By this means it is difficult to fabricate devices with channel spacing less than 100GHz. Phasars and etched gratings [15] have good, uniform insertion losses, but may not have satisfactory temperature control and polarization sensitivity, depending on the composite materials. Ruled diffraction gratings have low, uniform insertion loss, and excellent isolation; further, the complexity and cost of packaging do not increase significantly when the number of channels increases [29-34]. In this chapter, we discuss two kinds of 32-channel 100 GHz DEMUXs based on echelle gratings. One of them has single-mode input and

multimode output which can work as the bridge between optical backbone and metropolitan area networks. The other DEMUX has one input single-mode fiber, and 32 output single-mode fibers. The second approach is desirable for telecommunications networks because of the excellent qualities of single-mode fiber for long distance communications. Section 6.1.1 will show the optical design of the single-mode-in, single-mode-out device. Followed by the packaging process description (Section 6.1.2), non-linear effect discussion (Section 6.1.3) and the performance report (section 6.1.4).

The optical design and performance of a passband broadened single-mode-in and single-mode-out 32-channel 100GHz DWDM is given in section 6.2.1, 6.2.2. Finally, the summary is given in Section 6.3

6.1 A 32-channel 100 GHz single-mode-in, multimode-out DWDM

6.1.1 Device configuration and optical design

A simplified diagram of the optics of the DEMUX is shown in Figure 6.1. Thirty-two-channel WDM wavelengths are introduced into the DWDM device by a single-mode fiber with an FC connector, and then are collimated by a two-element lens. The same lens functions as the focusing lens for the demultiplexed signals. We used a 22nd-order echelle grating to demultiplex 32 optical signals within the C band with 100-GHz channel spacing. The working wavelength range of operation is from 1541.37 to 1565.47 nm. A 22nd order grating having the same parameters as described for the eight-channel multimode device in Chapter 4 was used here. The blaze angle

was 64° , the incident angle equals to diffraction angle that was 64.1° at the center wavelength of 1554.93 nm. The grating efficiency varies from 48% to 80% across the whole wavelength range. This grating gave us high dispersion, low polarization dependent loss (PDL), and relatively high diffraction efficiency. The ITU fiber-optic telecommunications channel standard [90, 91] determined the wavelength choice. In order to eliminate multiple alignments for individual fibers and to increase throughput, we employed a 32-channel silicon V-grooved fiber array to receive the 32 demultiplexed signals. The input fiber array, which has only a single fiber, sits directly on the top of the output fiber array. The input fiber is aligned with the center of the optical axis. This over/under configuration allows for better optical performance and a slightly smaller lens field of view than one in which the input fiber is at the end of the row of output fibers. The optical performance is better because the input fiber is near the optical axis of the lens, rather than being far from it, as in the other case. The core size of the multi-mode glass fiber is $62.5\ \mu\text{m}$. This DWDM device is designed for optical communications for metropolitan-area networks where free-space DWDM and multi-mode fiber band networks are jointly employed [65].

6.1.2. Demultiplexer Packaging and Performance

We used active alignment in the whole packaging process. It is critical to locate the focal point of the lens and to set the input fiber array exactly at the focal plane. We used a stage with 5 degrees of freedom to actively align the grating. We found the position of highest diffraction efficiency for the grating by fine-tuning the rotation

and the pitch of the grating. To arrive at its highest and most balanced coupling efficiency, we simultaneously monitored the output of the two end channels and the center channel, i.e., the 1st channel, the 18th channel, and the 32nd channel, at wavelengths of 1541.37 nm, 1554.93 nm, and 1564.47 nm respectively. In this way the alignments for other channels can be optimized automatically.

Figure 6.2 shows the output spectrum of the 32-channel DWDM. This figure indicates that the output signals of the 32 channels are quite uniform. The output spectrum was measured by a laser rather than a by wide-band white light source, so it shows the center wavelength of each individual channel rather than the exact loss spectrum, because of the narrow line-width of the laser. Insertion loss is defined as the difference between the input power of the DWDM device and the output power via the silicon V-grooved fiber array. This loss includes the loss of the input single-mode fiber, the lens, the grating, the silicon V-grooved fiber array, the connectors, and the coupling loss from free space to the output fiber array. Adjacent crosstalk is the power ratio between a specific channel and its adjacent channels when only that given channel is activated. Figure 6.3 shows the measurement of insertion loss for all 32 channels, which is also quite uniform across channels. Our measurements showed the typical insertion loss of this WDM system to be -3.0 ± 0.2 dB. Typical adjacent channel crosstalk is -30 dB among all 32 channels. The final packaging size was 6.2×2.4×1.5 inch.

When all the channels are aligned, we tuned the wavelength of individual channel, and found the average 1-dB optical passband of the 32 channels to be 0.256 nm. Figure 6.4 shows the 1-dB optical passband of all channels. The 1-dB passbands of all 32 channels vary from 0.22 nm to 0.31 nm, because the quality of the output light spot varies at different channels. The average value of the 1-dB passband is 0.256 nm. Because WDM laser sources usually contain a spectral width that depends on laser cavity structures and on operating conditions, laser wavelength shift is also present when the laser is internally modulated [67]. The relatively large 1-dB optical passband makes our DEMUX robust to the disturbance caused by laser wavelength shift. When all the channels are aligned and minimum insertion losses are achieved, the output fiber array is moved laterally every $2\mu\text{m}$ to the left and to the right side of a specific channel until the insertion loss increases by 1-dB. We measured the 1-dB passband of all channels as a function of lateral misalignment. The experiment supports the conclusion that the WDM system can tolerate lateral misalignment up to $30\mu\text{m}$ while maintaining a better than 0.256 nm 1-dB passband for all 32 channels.

Figure 6.5 shows the measurement of the 1dB physical passband for Channel 32, corresponding to $30\mu\text{m}$ lateral misalignment. This large dynamic range makes the device highly robust against any displacement of output fiber array caused by misalignment, temperature fluctuation, or vibration. Employing a specially made single-mode fiber array, and thereby decreasing fiber-to-fiber spacing by half, we

were able to use the same configuration to realize a 64 channel DWDM with 50-GHz spacing.

6.1.3 Simulation and experimental results of the fiber array's lateral movement tolerance

The wavelength shift of a specific channel causes the image of the input light spot to move accordingly. By using Equation (4.13), we can obtain the maximum movement tolerance of the WDM system when operating within the 1-dB passband range. We did simulation for two cases. In one case, the diameter of the input light spot $d = 9 \mu\text{m}$; in the other, $d=44 \mu\text{m}$. Figure 6.6 shows the simulation result, which indicates that when a system is diffraction-limited, *i.e.*, the input spot size is the same as the single-mode fiber core diameter; the maximum lateral movement tolerance can be up to $\pm 29 \mu\text{m}$ within the 1-dB passband.

An average of $\pm 15 \mu\text{m}$ lateral movement tolerance was demonstrated in our experiment, a result which agrees with $d=44 \mu\text{m}$, representing the worst spot quality that we found in our lens-design simulation. The lens used in our WDM system is a two-element lens. We can certainly achieve larger lateral movement tolerance by using more elements to obtain a diffraction-limited system.

6.1.4 Non-linearity performance of the device when working at ITU standard wavelength

By combining Equations (4.2) and (4.3), we can simulate the relationship between angular dispersion and wavelength. The result is shown in Figure 6.7. The 32-channel

designation on the x -axis of the figure corresponds to the 32 wavelengths, which are determined by the ITU grid. We found that the angular dispersion increases when the wavelength increases, and that therefore the channel spacing depends on wavelength. Figure 6.8 shows the simulated channel spacing of the 32 wavelengths, which fit exactly within the ITU grid. We found the channel spacing to vary from $115\mu\text{m}$ to $135\mu\text{m}$ across all 32 channels. When building the 32-channel prototype DEMUX, we tuned the individual wavelengths slightly to eliminate the non-linear effect of angular dispersion. We could make the wavelengths to fit exactly within the ITU grid by using nonlinear spaced V-grooved fiber array.

6.2 A 32-channel 100 GHz single-mode-in, single-mode-out DWDM

6.2.1 Device structure and optical design

We designed and built another 32-channel demultiplexer with one single-mode-input fiber and 32 single-mode-output fibers using the same structure as that in Section 6.1, but with different optical design. For telecommunications networks, single-mode DWDMs have been employed exclusively [31-33]. The major goal of this design is to have a pass band-broadened single-mode DWDM to compensate for the wavelength drift of lasers. Figure 6.9 shows the simplified schematic drawing of this demultiplexer (one layer). The major difference between this DEMUX and the one in Section 4.1 is that a graded-index lensed fiber array was used here to increase the filling ratio. The mode field diameter of graded-index lensed fiber can be expanded up to $45\mu\text{m}$, thus reducing the lateral and longitudinal misalignment

sensitivities [92,93]. The detailed design and analysis of graded-index lens fiber will be given in Chapter 7. The one-layer fiber array has one input single-mode fiber and 32-single-mode output fibers. The spacing of the fiber array was designed to be non-uniform varying from 140.1 to 164.4 μm to obtain accurate center wavelength within the ITU grid.

Figure 6.10 shows the optical layout of the demultiplexer. This three element lens was designed for a 50-channel 100-GHz spaced-DEMUX covering wavelength range from 1528.63 to 1567.53 nm. The focal length is 72.5mm. The grating is tilted at 62.7° . The incident angle equals to the diffraction angle, which was 62.7° at the center wavelength 1555.73nm. The whole optical design was done using optical design software ZEMAX. The spot diagrams for channel 1, 2, 25, 49, 50 are shown in figure 6.11. The spots across the whole wavelength range are diffraction limited. The average light spot diameter is $10\mu\text{m}$, much smaller than the core size of graded-index lensed fiber. This factor eased the lateral and longitudinal alignment greatly. Since the mode field diameter of this special fiber was increased, the numerical aperture is decreased to 0.032 restricting the tolerance of the angular alignment. This demultiplexer was fully packaged. The final packaging size was $10.5 \times 3.0 \times 0.9$ inch.

6.2.2 Device performance

A 32-channel single-mode-in and single-mode-out demultiplexer was actually built and tested. The spectral passband of the 32-channel WDDM is shown in Figure 6.12 as measured with an ASE source. The average insertion loss was 4.5 dB, and the

standard deviation was 0.74dB. The wavelength accuracy is within 0.078 nm. The 1db passband varied from 0.09 to 0.16 nm, and the 3dB passband varies from 0.16 to 0.26 nm. The variation among channels was mainly due to the non-uniform spacing of the fiber array (varying from 140.1 to 164.4 μ m from one end to the other). The theoretical 3dB passbands varies from 0.219 to 0.257 nm. This outcome was in relatively good agreement with the experimental results. The average measured 3dB passbands (0.2 nm) was slightly smaller than the theoretical ones (0.23 nm). This difference is because it is quite difficult to control the exact position of the front faces of individual fibers during silicon fiber array fabrication. Also, polishing after fabrication might also cause the length of the graded-index fiber to be smaller than designed. The passband is much better than simply using standard single-mode fibers as output fibers. The theoretical 3dB passband of 100GHz DWDMs using standard single-mode fibers is only 0.06 nm. (See Chapter 7.1) The average crosstalk is – 51dB, which is the best channel isolation so far achieved by all kinds of technologies. The average PDL is 0.36 dB. Table 6.1 shows the detail measurement results for wavelength; insertion loss; passband at the 1-dB, and 3-dB points; crosstalk; and polarization independence loss. This device was designed for telecommunication networks which require 10Gbps minimum bit rate. The theoretical maximum data transmission bit rate was calculated by combining Eqs. (4.9) & (4.12). The result was 33Gbps. We measured the data transmission bit rate of this single-mode DEMUX using a similar setup as Figure 4.8. The difference was that there was no mode

scrambler and the maximum signal speed of the signal generator was 12.5Gbps. Figure 6.13 shows a clearly opened eye diagram of this device, when the input signal was modulated at 12.5Gbps. The ratio of signal to noise was 7.43.

6.3 Chapter 6 Summary

We designed, built, and tested two fully packaged 32-channel 100-GHz demultiplexers. For the single-mode-in, multimode-out model, the insertion losses of all 32 channels were within -3.0 ± 0.2 dB. The crosstalk between adjacent channels for all channels is close to -30 dB. The average 1-dB optical passband is 0.256 nm, making the device robust against disturbances caused by wavelength and temperature fluctuations.

For the single-mode-in and single-mode-out device, especially designed graded-index lensed fibers were applied to expand the mode field diameter, and then to increase passband and alignment tolerance. The average insertion loss is 4.5dB; the crosstalk between adjacent channels is -51 dB; the average 1-dB, and 3-dB passbands are 0.11 nm, and 0.2 nm respectively, much better than that of simply using standard single-mode fibers.

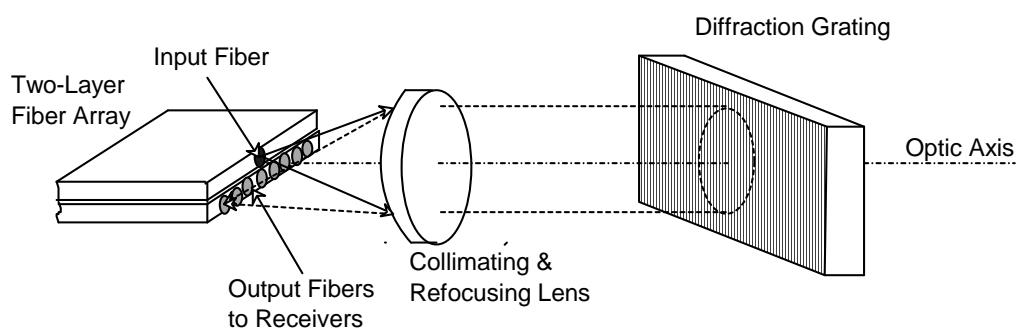


Fig. 6.1 Schematic optical layout of the 32-channel single-mode-in, multimode-out demultiplexer

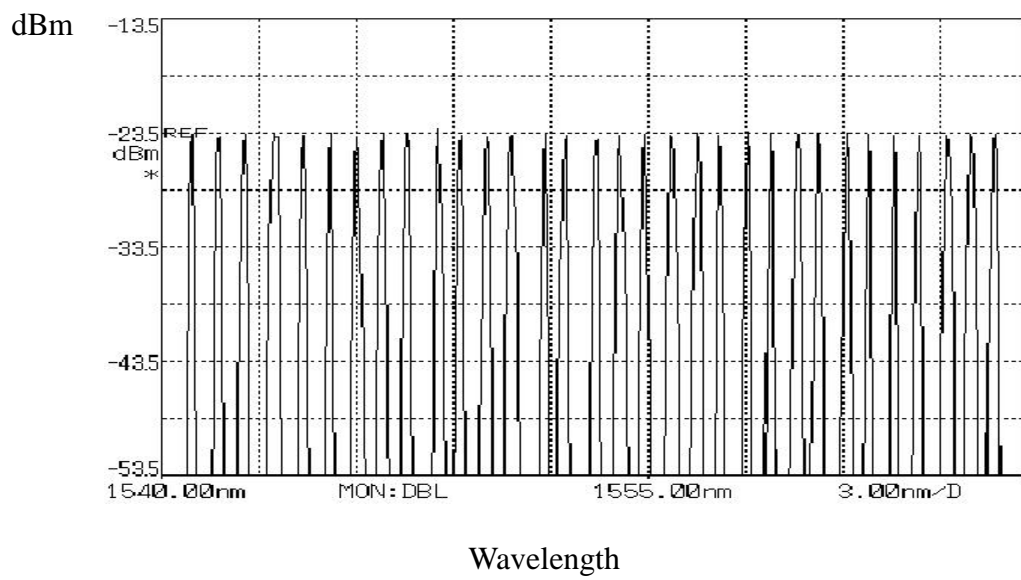


Fig. 6.2 Output spectrum of the 32-channel demultiplexer

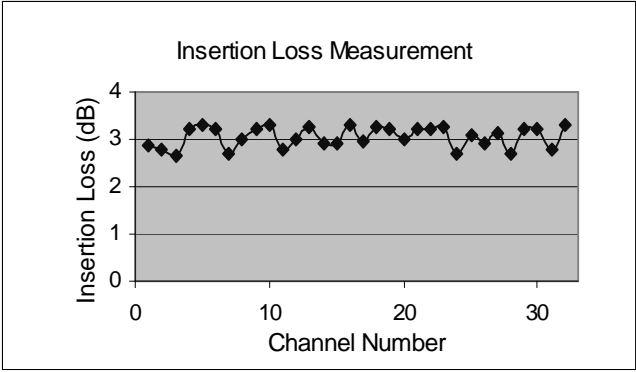


Fig. 6.3 Insertion loss measurement results for all 32 channels

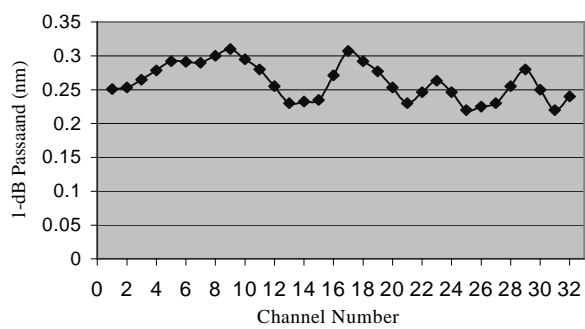


Fig. 6.4 1-dB optical passband measurement results.

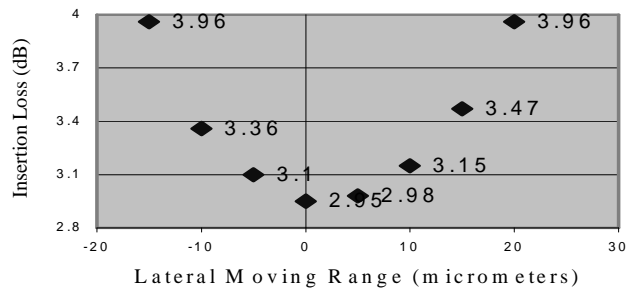


Fig.6.5. 1-dB physical passband measurement for Channel 32. When lateral movement reaches 15 μ m to the left or 20 μ m to the right side of the center of Channel 32, insertion loss increases by 1 dB.

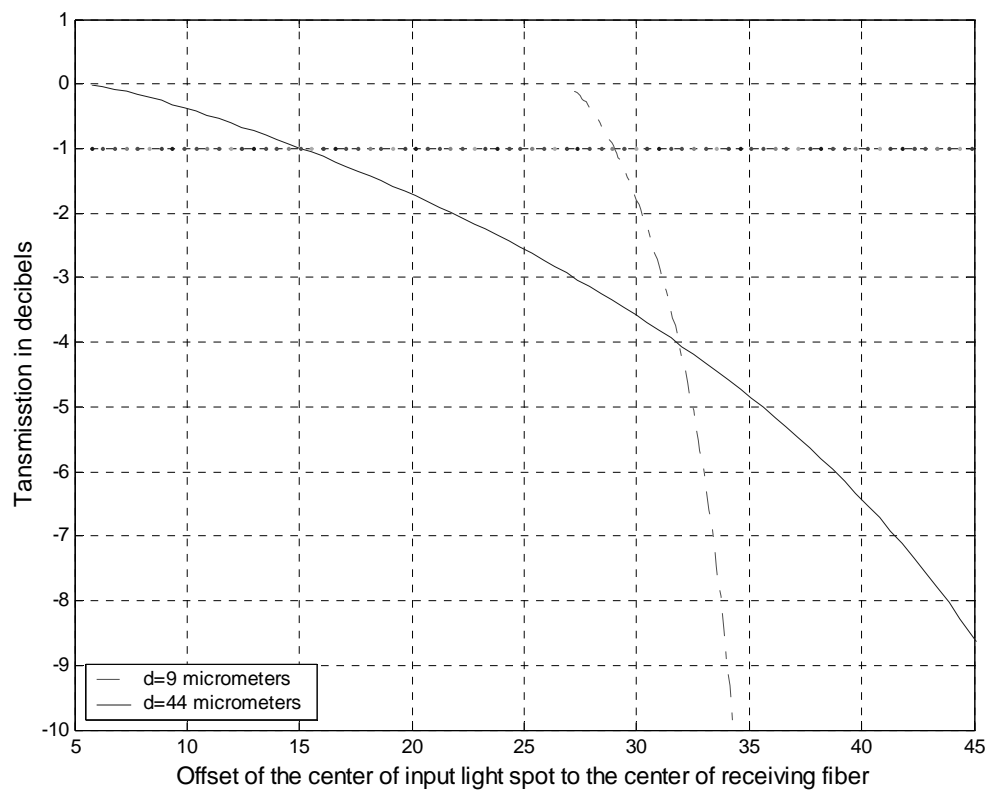


Fig.6.6 Simulation results of transverse loss versus offset of fiber cores with different transmitting spot size.

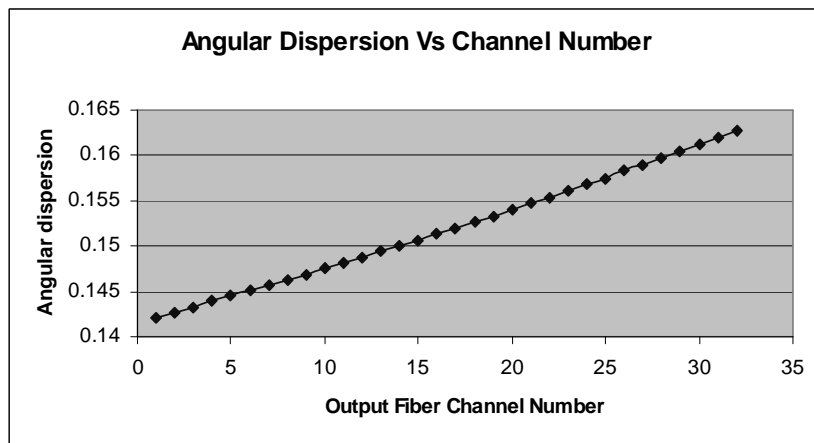


Fig. 6.7 Angular dispersion at different wavelengths. This graph shows that the larger the wavelength, the greater the angular dispersion. (Larger channel number corresponds to longer wavelength.)

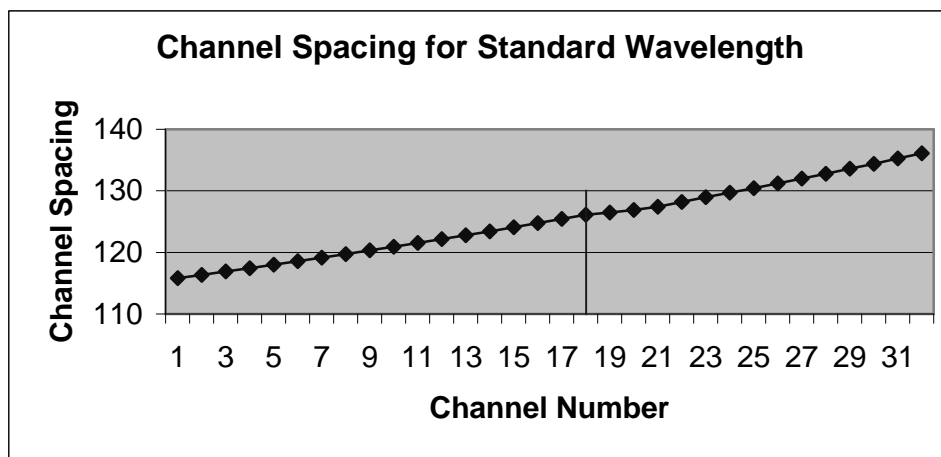


Fig 6.8 Unequal channel spacing caused by the non-linearity of angular dispersion

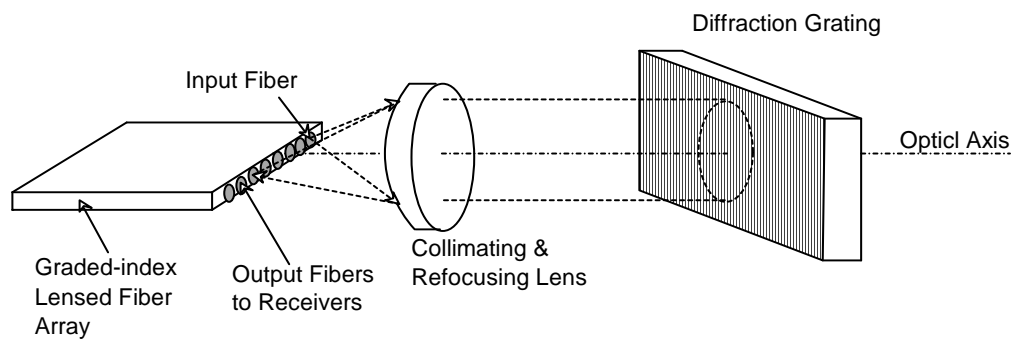


Fig.6.9 The simplified schematic drawings of a 32-channel single-mode-in and single-mode-out DWDM.

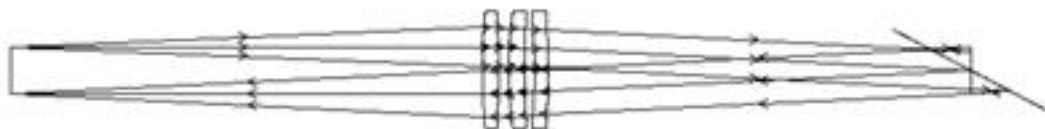


Fig. 6.10 The optical layout of the demultiplexer. All the optical designs for lens, fiber array, and grating are good for demultiplexing 50 wavelengths covering the whole C band.

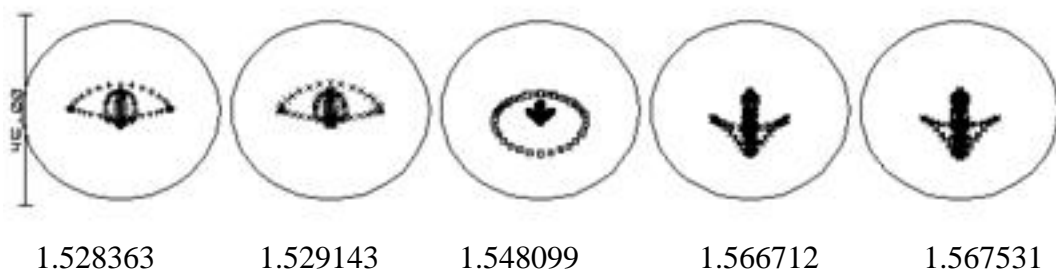


Fig. 6.11 The spot diagram for the diffracted wavelengths at two ends and the middle of the spectral range. The circles outside of individual spots represents the core size of GILF

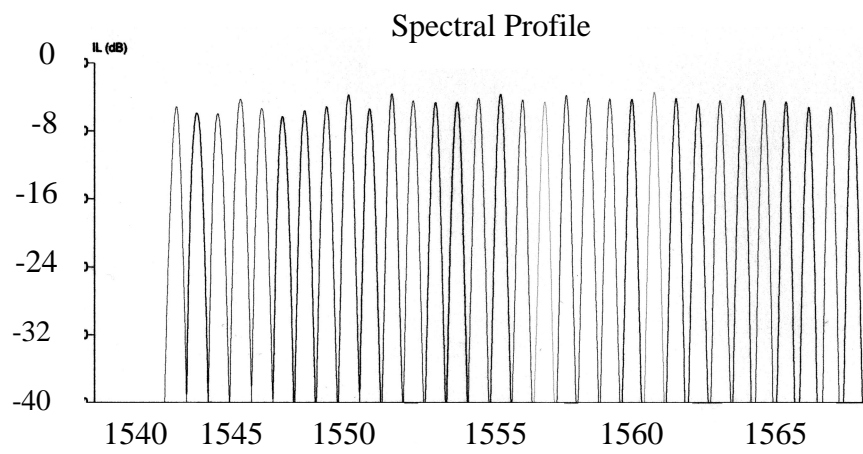


Fig. 6.12 Output spectrum of the 32-Channel single mode DWDM

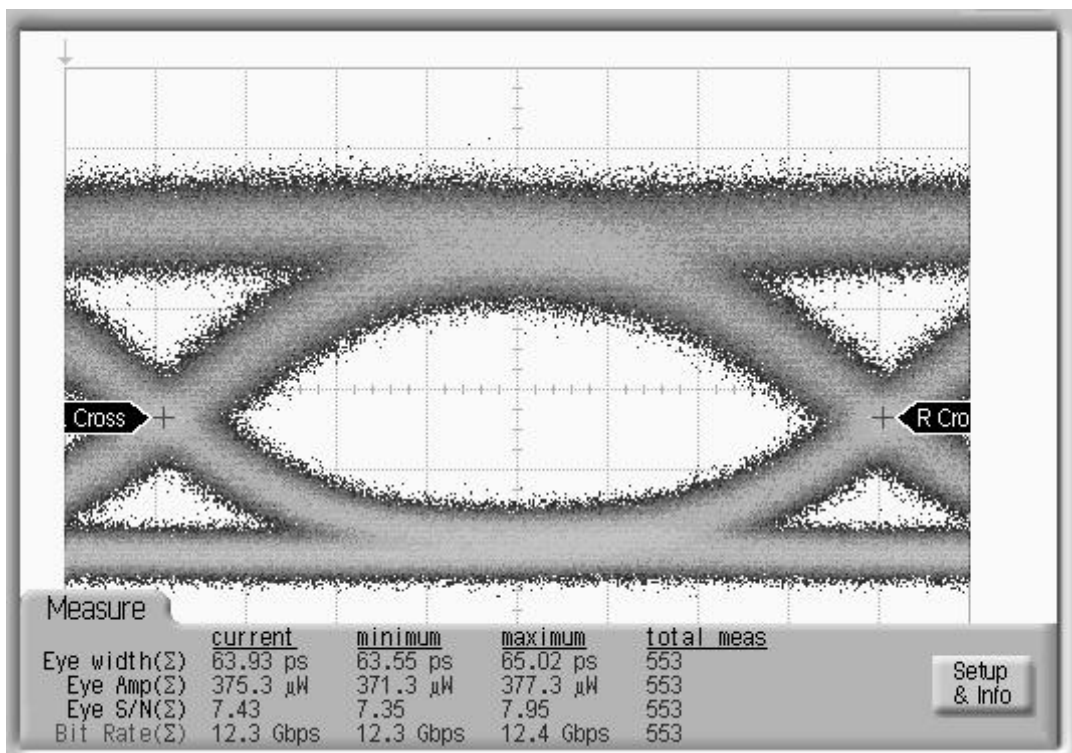


Fig. 6.13 The eye diagram of the 32-channel DEMUX when input single signal was modulated at 12.5Gbps. The signal to noise ratio was 7.43.

Table 6.1 Detailed measurement results for individual channels

	Design Wavelength (nm)	Measured Wavelength (nm)	Difference (nm)	Insertion Loss (dB)	BW1: @ 1.00 dB (nm)	BW2: @ 3.00 dB (nm)	Crosstalk (dB)	PDL (dB)
1	1567.9522	1567.953	0.0008	3.874	0.101	0.179	49.77	0.828
2	1567.1312	1567.132	0.0008	5.099	0.093	0.164	50.09	0.821
3	1566.3138	1566.324	0.0102	5.148	0.097	0.168	48.99	0.767
4	1565.4959	1565.482	-0.0139	4.467	0.095	0.167	50.23	0.74
5	1564.6788	1564.683	0.0042	4.316	0.096	0.168	49.84	0.681
6	1563.8626	1563.881	0.0184	3.749	0.105	0.176	52.76	0.672
7	1563.0472	1563.052	0.0048	4.336	0.1	0.177	50.81	0.618
8	1562.2327	1562.244	0.0113	4.724	0.105	0.185	50.84	0.577
9	1561.4191	1561.43	0.0109	4.108	0.101	0.173	51.61	0.552
10	1560.6062	1560.627	0.0208	3.361	0.109	0.183	54.03	0.482
11	1559.7943	1559.802	0.0077	4.191	0.102	0.177	53.15	0.449
12	1558.9831	1558.981	-0.0021	4.127	0.097	0.177	52.13	0.414
13	1558.1729	1558.192	0.0191	4.053	0.108	0.188	51.71	0.378
14	1557.3634	1557.378	0.0146	3.71	0.099	0.173	54.8	0.362
15	1556.5548	1556.584	0.0292	4.487	0.099	0.172	53.78	0.313
16	1555.7471	1555.768	0.0209	4.231	0.099	0.171	53.97	0.256
17	1554.9401	1554.959	0.0189	3.61	0.109	0.19	54.89	0.269
18	1554.134	1554.146	0.012	4.059	0.113	0.199	53.2	0.197
19	1553.3288	1553.36	0.0312	4.52	0.123	0.206	50.88	0.176
20	1552.5244	1552.558	0.0336	4.552	0.11	0.193	50.79	0.13
21	1551.7208	1551.736	0.0152	4.372	0.11	0.191	52.51	0.099
22	1550.918	1550.956	0.038	3.546	0.104	0.185	51.6	0.067
23	1550.1161	1550.13	0.0139	5.357	0.123	0.216	48.95	0.013
24	1549.315	1549.357	0.042	3.703	0.119	0.206	52.03	0.068
25	1548.5148	1548.55	0.0352	5.079	0.121	0.205	48.32	0.078
26	1547.7153	1547.742	0.0267	5.554	0.123	0.211	48.12	0.096
27	1546.9167	1546.927	0.0103	6.236	0.132	0.231	49.09	0.141
28	1546.1189	1546.16	0.0411	5.288	0.133	0.223	47.22	0.186
29	1545.3219	1545.375	0.0531	4.236	0.144	0.24	49.95	0.218
30	1544.5258	1544.539	0.0132	5.909	0.135	0.235	49.07	0.26
31	1543.7305	1543.768	0.0375	5.866	0.157	0.26	46.14	0.297
32	1542.936	1543.014	0.078	5.104	0.116	0.206	46.55	0.299
Ave.			0.02055	4.5304	0.1118	0.1936	50.8694	0.36

Chapter 7: Optimized Optical Design for Passband Broadening and Nonlinear Correction of Angular Dispersion

7.1 Passband broadening

Broadening and flattening of the passband in WDM is a key to maximizing spectral efficiency and relaxing the tolerance on wavelength control in the networks [94]. Typical grating-based WDMs have passbands or spectral responses that are generally highly peaked with a slow roll-off in their wavelength response. This effect results from the diffraction response of the associated grating element that separates the wavelengths, from the transmission response of intervening optical lens elements, and from the receiving optics. Such responses do not use the full bandwidth of most multiplexers and demultiplexers. As a result, it is often difficult to specify wavelength tolerances for associated components such as laser light sources, amplifiers and other optical components.

The width of the optical passband is mainly determined by the filling ratio “ F ”, *i.e.*, the ratio of the receiving fiber core diameter to the distance between the centers of two neighbor fibers. The larger this ratio, the larger the passband. In order to increase passband, one can either increase the core diameter or decrease the central spacing between adjacent output fibers. The output image reshaping and broadening approach [95,96] has been used for array waveguide-based WDM. For diffraction grating based WDM, in order to increase core diameter or increase mode field diameter (MFD), one can use thermal expanded core fibers [97, 98], use graded-index

lensed fibers [99-102], or defocus the focused beam spots at the focal plane [103]. In order to decrease the fiber spacing, we can strip the coating or etch the cladding to the smallest allowable size. But one can neither increase the core diameter nor decrease the channel spacing without limitation. There is an intrinsic trade-off between passbands and crosstalks. A lower crosstalk implies a wider separation between the output fibers and, therefore, necessarily higher linear dispersion, resulting in proportional bandwidth narrowing.

The Littrow mount geometry of our WDM design provided aberration-free image systems. The light spots of diffracted beams are almost identical in size to the cores of the fibers. In this case, the optimized value of this ratio $F=0.667$ [104].

Figure 7.1 shows the geometrical layout of the fiber array. D is the fiber cladding diameter, d is the fiber core diameter; and b is the distance between the centers of two adjacent fibers. For the most compact fiber array layout, $b=D$. For typical single-mode fibers, the value of d is approximately $9.5 \mu\text{m}$; cladding diameter D is $125 \mu\text{m}$, meaning that b is usually no smaller than $125 \mu\text{m}$. The resulting filling ratio is:

$$F = \frac{9.5}{125} = 7.6\% \quad (7.1)$$

For a 100-GHz (0.8nm) single-mode DWDM, the corresponding 3dB passband is only 0.06nm. Generally we need a 0.2nm 3-dB passband to compensate the wavelength shift in laser sources. Thus it is of the utmost importance to find solutions for broadening the passband of grating-based single-mode DWDM.

The typical value of “ d ” of multimode fiber is $62.5\mu\text{m}$, the value of “ b ” is

125 μm . Therefore, the resulting filling ratio for multimode fiber is:

$$F = \frac{62.5}{125} = 0.5 \quad (7.2)$$

The filling ratio of the multimode DWDM is superior to that of single mode devices.

For a 100GHz multimode DWDM, the corresponding 3dB passband is 0.4nm.

7.2 Design of Graded-index lensed fibers (GILFs)

Cascading a graded-index fiber (GIF) to a single-mode fiber to either expand or reduce the MFD of the single mode fiber has been reported for fiber/waveguide [100] and laser/fiber coupling [101]. For WDM application, we can use GIFs as spot expander to increase the 1dB optical passband.

Figure 7.2 shows the beam propagation through lensed media following Kogelnik's ABCD law [105]. The input plane contains the end face of a single-mode fiber and the beam waist w_{in} ; the output plane contains the final beam waist w_{out} which is formed after passing through a square-law lensed medium. The square-law dependence of the refractive index of the lens media can be expressed as:

$$n(r) = n(1 - g^2 r^2)^{\frac{1}{2}}, \quad (7.3)$$

where, n is the refractive index on the lens axis; r is the radial position from the axis.

The focusing parameter g can be expressed as

$$g = \frac{\sqrt{2\Delta}}{r}, \quad (7.4)$$

where in, Δ is the relative refractive index difference between the core axis and its perimeter at r .

When the fiber-lens is fused to a single mode fiber directly, the final waist size and its location can be expressed as [106]:

$$w_{out} = \frac{\lambda}{ng\pi w_{in} (\sin^2(gd) + (\frac{\lambda}{\pi w_0^2 ng})^2 \cos^2(gd))^{\frac{1}{2}}}, \quad (7.5)$$

and

$$z_w = \frac{n_2(1 - (\frac{\lambda}{\pi w_0^2 ng})^2) \sin(gd) \cos(gd)}{ng(\sin^2(gd) + (\frac{\lambda}{\pi w_0^2 ng})^2 \cos^2(gd))}. \quad (7.6)$$

A quarter-pitch length of graded-index fiber acts as a collimator that can expand mode field diameters (MFDs) of single-mode fibers (SMFs). Figure 7.3 shows the direct cascading of a single mode fiber and a graded-index multimode fiber.

The period (1 pitch) of a ray trajectory is given by $2\pi/g$. Substituting the length of a quarter pitch $d=\pi/2g$ in Equations (7.5) and (7.6), yields $z_w=0$, and Equation (7.7) can be derived:

$$w_{in} w_{out} = \frac{\lambda}{\pi ng}. \quad (7.7)$$

This relationship indicates that the product of the input and output mode-field diameters is reci-proportional to focusing parameter g . If the input MFD is smaller than the fundamental MFD of the graded-index fiber (GIF) it will expand; if larger, it will contract. So g is a significant parameter. From Equation (7.4), we can find out the smaller the value of difference in refractive index Δ , the smaller g . Figure 7.4 shows the respective different output MFDs when varying the value of g and the MFDs of a

input fiber. If a standard single mode fiber (MFD=10.2 μm) is cascaded with a Corning multimode fiber having core diameter of 50 μm ($g=0.053$), the output MFD of GILF has a value of 24.3 μm ; if a standard single mode fiber is cascaded with a Corning multimode fiber having core diameter of 62.5 μm ($g=0.0057$), the output MFD of the GILF is 22.9 μm . This figure clearly shows that, when given the input MFDs, the smaller the value of g , *i.e.*, the smaller the value of Δ , the larger output MFDs we can obtain.

We also calculated different output MFDs by varying the MFDs of input fibers while keeping the same value for g . For instance, if dispersion-shift fibers (DSFs) which have a smaller MFD (7.6 μm) are cascaded to specially-made graded-indexed fibers (GIFs) ($g=0.0033$), larger output MFDs (57 μm) were obtained. On the other hand, if standard single-mode fibers are cascaded to the same GIFs, the output MFDs are only 40 μm . When we decrease the value of g to 0.028, the output MFDs can reach 47 μm . The conclusion then is that DSF or GIF with a smaller value of g are always preferable to expand the output MFDs in GILF design.

The GILFs in our WDM design have MFDs of 45 μm . Section 6.2.2 confirmed that a maximum 0.256nm 3-dB passband had been achieved in a 32-channel single-mode-in and single-mode-out DWDM.

7.3 Cylindrical lens for passband broadening

Various techniques may be used to defocus multiple wavelength optical signals to achieve some spectral broadening. Previously available defocusing techniques [103]

and procedures generally create significant losses due to spreading of the multiple wavelength signals in directions which are both parallel and perpendicular to the direction of dispersion. Therefore, defocusing of multiple wavelength optical signals has generally been avoided in most optical communications systems.

For the 200GHz eight-channel multimode DWDM described in Chapter 4, an improved optical design has been done to increase the optical passband. A spectral modifying-element cylindrical lens was used to preferably defocus or spread optical signals only along the direction of dispersion of diffraction gratings to provide desired spectral broadening or passband broadening without increasing much signal loss level as compared with conventional defocusing techniques. Figure 7.5 shows the broadened and flattened oval-shaped profiles of output light spots after adding the cylindrical lens mentioned above. We also etched the cladding of the output fiber down to 90 μ m in order to further increase the filling ratio. The optical design is shown in figure 7.6. It is a three-element diffraction limited-lens design, a concave-plano cylindrical lens with a curvature of -7324mm on the left surface. A thickness of 5mm was inserted 5mm behind the third element. Figure 7.7 shows the transmission spectrum of the eight-channel 200GHz multimode DWDM both with and without the cylindrical lens. Figure 7.7 clearly shows that the passband is broadened by adding this cylindrical lens, but it does introduce 1dB of extra insertion loss. The total average loss will be around -3.5dB. Table 7.1 shows the passband value at different loss levels with and without the cylindrical lens. At -0.5dB insertion loss point, the

passband was increased from 0.2nm to 0.4nm. The crosstalk is -30dB at the 3-dB point. The major advantage of this design is that adding the cylindrical lens does not affect the devices' focusing. The cylindrical lens can be inserted or removed according to passband requirement.

7.4 40-Channel single-mode demultiplexer using a thermally-diffused expanded-core fiber array with uniform spacing

Thermally-diffused expanded core (TEC) techniques allow the fabrication of fibers with their mode fields expanded by the thermal diffusion of core dopants [97,98]. The TEC fiber is fabricated by micro-flame heating. The dopants distributed in the fiber determine the core region. The concentrated dopants will spread along the radial axis by thermal diffusion when the fiber is heated. As a result, the core region diameter becomes larger than the original diameter. The core expansion rate depends on dopant intensity in the core of the fiber, on the heating temperature, and on heating time. Figure 7.8 shows the schematic diagram of a TEC fiber. The adoption of a larger mode field diameter in single-mode WDM design certainly will reduce the stringent requirements on optical alignment and broaden the optical passband [92,93].

We designed a 40-channel 100-GHz single-mode-in, single-mode-out DWDM to further improve passband and correct the nonlinear effect of angular dispersion. The frequency operating range is from 192.2 to 196.1THz. Figure 7.9 shows the optical layout of this demultiplexer. The working principle is the same as our previous grating-based WDM design. There are two major improvements in this design. a)

TEC fibers with MFDs of $40\mu\text{m}$, cladding diameter of $73\mu\text{m}$ were installed in a silicon V-grooved fiber array. b) The fiber array had almost uniform channel spacing of $75\mu\text{m}$. The filling ratio was increased from 7.6% to 53%. Figure 7.10 shows the comparison of the spectral profiles using TEC fibers and SMFs. The profile of the TEC fiber is much broader than that of the SMF. The simulation results from ZEMAX showed 0.26nm 1-dB passband and 0.44nm 3-dB passband.

In order to make DWDM working at the ITU grid, which requires uniform frequency spacing, we either need to use fiber array having non-uniform channel spacing or to improve the optical design to correct the nonlinear effect of angular dispersion [29,54]. We designed a DWDM (see Section 6.2) with fiber array having non-uniform spacing so that we could obtain accurate central wavelength for individual channels, but it also gave us non-uniform optical passband. In this new design, a concave lens tilted at 12° was inserted 2mm away from the front face of a TEC fiber array to correct the non-linear angular dispersion effect. The tilt angle, curvature, and thickness of this concave tilt element were obtained by using the optimization function of ZEMAX. These three parameters together with the thickness, curvature of other lens elements were set as variables; a uniform channel spacing of $75\mu\text{m}$ and diffraction limited output spot quality were set as the targets of the merit functions in the optimization process. Figures 7.11(a) and 7.11(b) show the simulated channel spacing of the fiber array without and with nonlinear correction respectively. Figure 7.11(a) shows that the channel spacing varies from 75 to

95.74 μm when there is no nonlinear correction. The variation is 21.67%. Figure 7.11(b) shows that the channel spacing varies from 74.68 to 75.86 μm when using nonlinear correction. The maximum variation is 1.18 μm , which corresponds to a 0.0126nm wavelength shift. The relatively large 1-dB pass band (0.256nm) achieved from this design can definitely tolerate this small wavelength shift without suffering appreciable insertion loss.

7.5 Chapter 7 Summary

Three kinds of techniques used to broaden the optical passband have been reported in this chapter. Both GILF and TEC fibers expanded the core diameter to increase the filling ratio. The pitches of fiber arrays were decreased by stripping coatings and etching claddings.

The 3-dB passband of GILF-based single-mode DWDM was increased from 0.06nm to 0.2nm. The 3-dB passband of the TEC fiber-based single-mode DWDM reached 0.44nm by further etching the cladding down to 73 μm .

A cylindrical lens was inserted into a DWDM optical design to supply defocusing along the grating dispersion. For a 200-GHz spaced multimode DWDM, the 1-dB passband can be enlarged from 0.4nm to 0.6nm, and the 3-dB passband can be enlarged from 0.8nm to 1nm. The minimum channel spacing for this design was 90 μm .

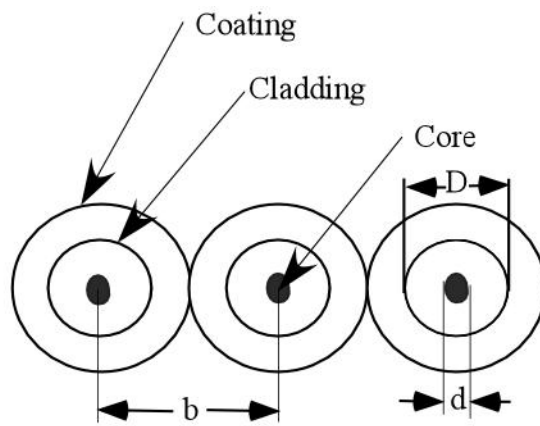


Fig. 7.1 Geometrical layout of fibers in a compact fiber array

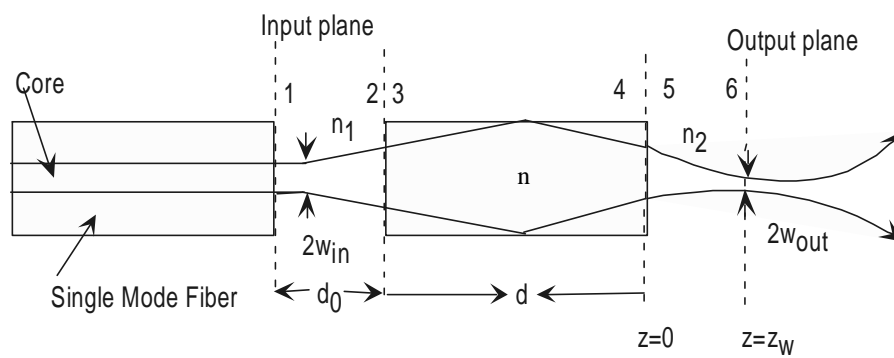


Fig. 7.2 Beam propagation through lensed media following Kogelnik's ABCD law

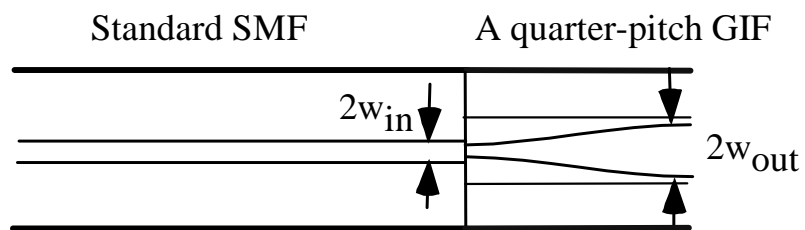


Fig.7.3 Cascading a SMF with a quarter-pitch length of GIF

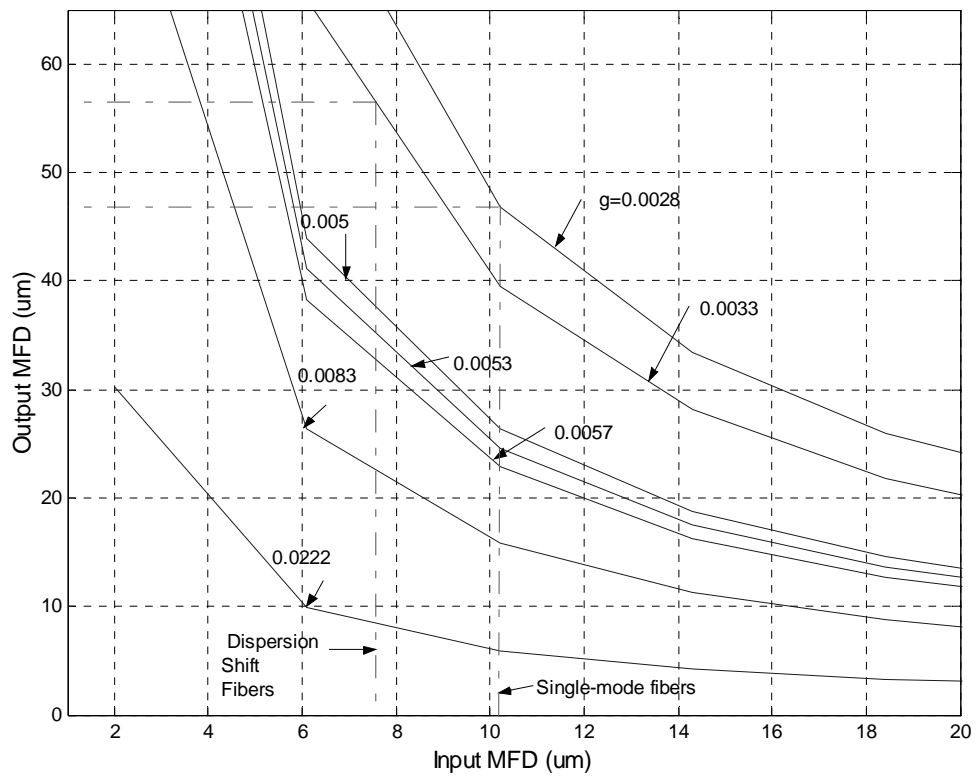


Fig. 7.4 Output MFD of a graded-index lensed fiber with a different value of g . When $g=0.0033$, for dispersion shift fibers (MFD of $7.6 \mu\text{m}$ at 1555nm), the output MFD is $57 \mu\text{m}$; for the standard single mode fiber (MFD= $10.2\mu\text{m}$), the output MFD is about $47\mu\text{m}$.

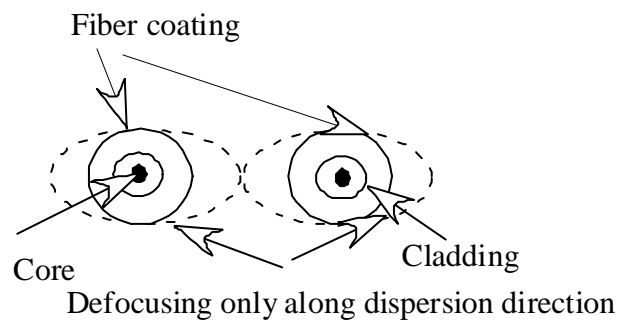


Fig. 7.5 The broadened and fattened oval-shaped profiles of output light spots after adding the cylindrical lens

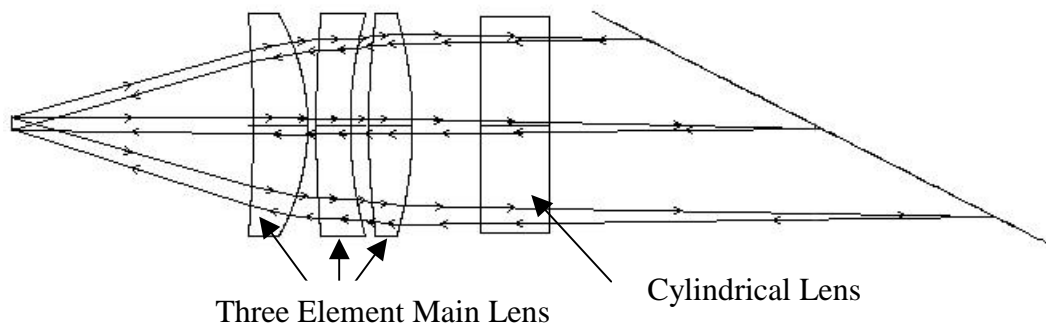


Fig. 7.6 Optical layout of a passband broadened 40-channel single-mode DWDM. A 5mm-thick cylindrical lens is inserted 5mm right of three-element main lens. The curvature of cylindrical is -7324mm , infinity for the left and right surfaces respectively. The nominal output fiber array spacing is $90\mu\text{m}$.

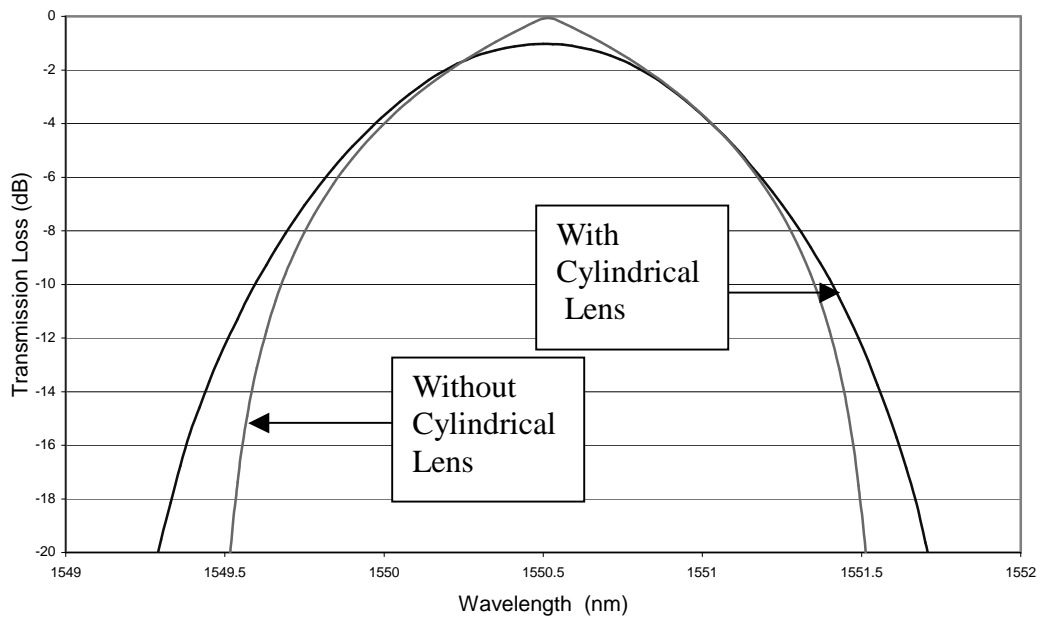


Fig. 7.7 Transmission spectrum of an eight-channel, 200-GHz multimode DWDM with and without the cylindrical lens

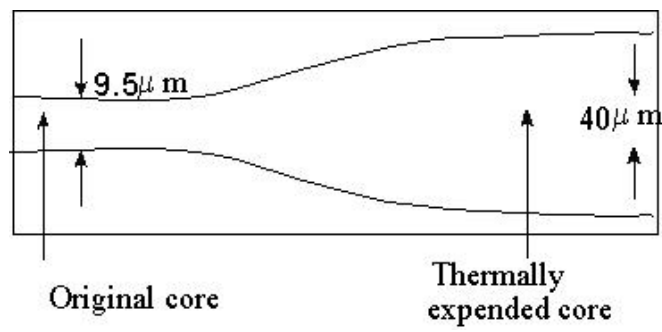


Fig. 7.8 The schematic diagram of TEC fiber. The concentrated dopants in the core region will spread along the radial axis by thermal diffusion when the fiber is heated. As a result, the core region diameter becomes larger than the original diameter.

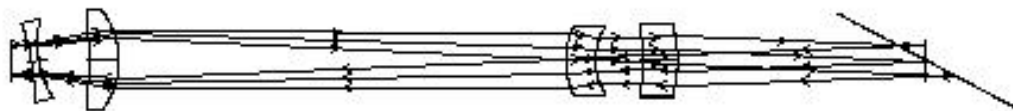


Fig. 7.9 Optical layout of a passband-broadened 40-channel single-mode demultiplexer with uniform fiber array channel spacing.

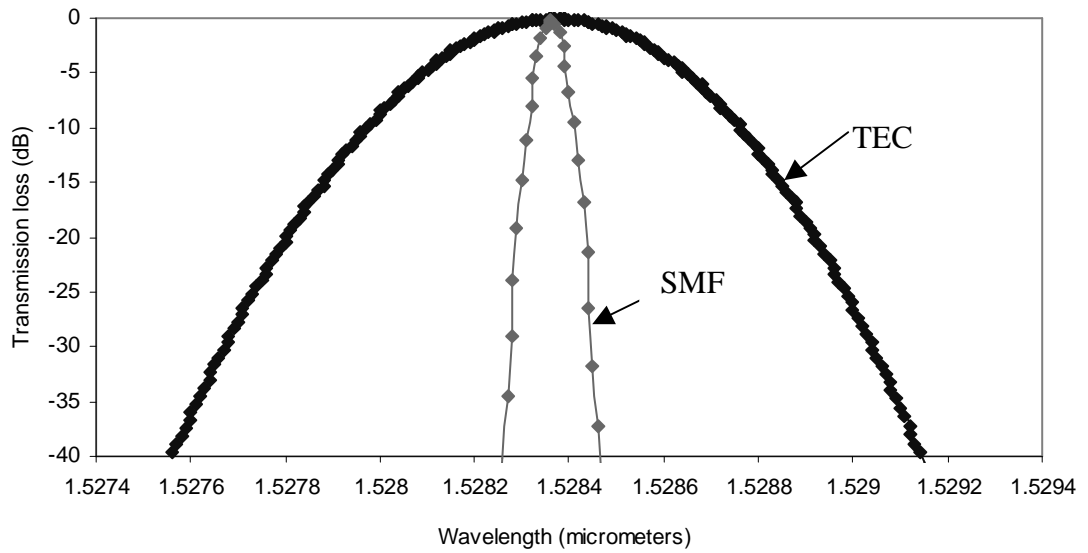


Fig. 7.10 Comparison of spectral profiles using TEC fiber and SMF. The profile of TEC fiber is much broader than that of SMF.

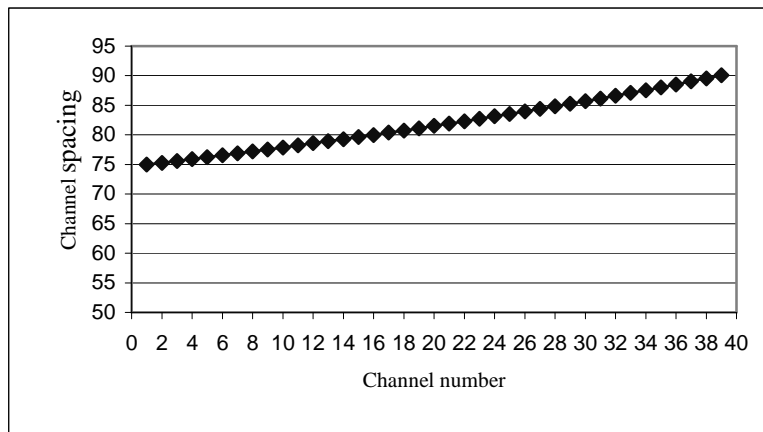


Fig. 11 (a)

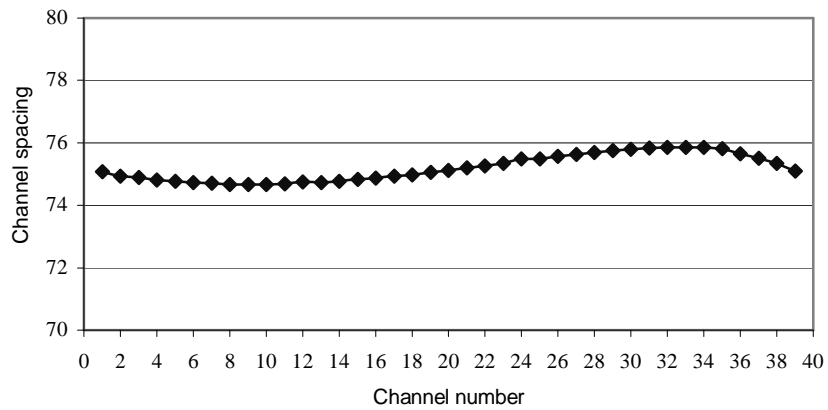


Fig. 11 (b)

Fig. 7.11 (a) Channel spacing of the fiber array without nonlinear correction
 (b) Channel spacing of the fiber array with nonlinear correction

Table 7.1 Passband at different loss level with and without cylindrical lens

Passband	Without cylindrical lens (nm)	With cylindrical lens (nm)
0.5 dB point	0.2	0.4
1 dB point	0.4	0.6
3 dB point	0.8	1

References

1. Rajiv Ramaswami and Kumar N. Sivarajan, *Optical networks: a practical perspective*, Morgan Kaufmann Publishers, 1998.
2. Green, P. "Progress in optical networking," *IEEE Communications Magazine*, **39** (1), 54 –61 (2001)
3. Lucent Technologies, "Dense wavelength division multiplexing (DWDM)," www.iec.org/online/tutorials/dwdm
4. V. Maxwell, "Optical networking," *IEEE Potentials*, **18** (1), 26 –28 (1999)
5. S. Tariq, M.K. Dhodhi, J.C. Palais, R.E.Ahmed, "Next generation DWDM networks: demands, capabilities and limitations," *Electrical and Computer Engineering, 2000 Canadian Conference on*, **2**, 1003-1007 (2000).
6. Lucent Technologies, "Lucent technologies demos record breaking 100-channel optical amplifier with potential to revolutionize optical networking technology," www.lucent.com/press/0797/970721
7. Lucent Technologies, "Lucent Technologies Bell Labs scientists report world's first long-distance transmission of trillion bits of data using 100 colors of light," www.lucent.com/press/0398/980302.bla.html
8. Lucent Technologies "Bell Labs uses ultra-dense WDM to transmit 1,022 channels over fiber," www.lucent.com/news/1999/november/10/2.html

Fiber nonlinear effects are a major and ultimate source of system limitations. These effects may determine launch power, repeaterless distance and maximum

number of channels. The major nonlinear effects in ultra-dense WDM system are four-wave mixing (FWM) and stimulated Raman scattering (SRS)

9. Jaafar M. H. Elmirghari, Hussein T. Mouftah, "Technologies and architectures for scalable dynamic dense WDM networks," *IEEE Communications Magazine*, 58-66 (2000)
10. M. S. Goodman, H. Kobrinski, M. Vecchi, R. M. Bulley, and J. M. Gimlett, "The LAMBDANET multiwavelength network: architecture, applications and demonstrations," *IEEE J. Select. Areas Commun.* **8**(6), 995-1004 (1990).
11. K. Nosu, H. Toba, K. Inoue, and K. Oda, "100 channel optical FDM technology and its applications to optical FDM channel-based networks," *IEEE/OSA Journal of Lightwave Technology.* **11**, 764-776 (1993).
12. N. R. Dono, P. E. Green, K. Liu, R. Ramaswami, and F. F. Tong, "A wavelength division multiple access network for computer communication," *IEEE J. Selected Areas in Commun.* **8**(6), 983-994 (1990).
13. F. J. Janniello, R. Ramaswami, and D. G. Steinberg, "A prototype circuit-switched multi-wavelength optical metropolitan-area network," *IEEE/OSA J. Lightwave Technol.* **11**, 777-782 (1993).
14. W. E. Hall, et al., "The rainbow-II gigabit optical network," *IEEE J. Select. Areas Commun.* **14**, 814-823 (1996).
15. Emil S. Koteles, "Integrated Planar Waveguide Demultiplexers for High Density WDM Application", *Wavelength Division Multiplexing*, Ray T. Chen, Louis S. Lome, SPIE PRESS, **CR71**, 3-32 (1999)

16. T.Mizuochi, K.Shimizu, T.Kitayama, "All-fiber add/drop multiplexing of 6 x 10¹⁰ gbit/s using a photo-induced bragg grating filter for WDM networks," *Optical Fiber Communications*, 116 –117 (1996)
17. Hee Su Park; Seok Hyun Yun; In Kag Hwang; Sang Bae Lee; Byoung Yoon Kim, "All-fiber add-drop wavelength-division multiplexer based on intermodal coupling," *IEEE Photonics Technology Letters*, **13** (5), 460 –462 (2001)
18. M.Ibsen, R.Feced, P.Petropoulos, M.N. Zerva, "99.9% reflectivity dispersion-less square-filter fibre Bragg gratings for high speed DWDM networks," *Optical Fiber Communication Conference, 2000* , **4** , 230 -232 (2000)
19. Loren F. Stokes, "Optical-fiber filters for wavelength division multiplexing," *IEEE Circuits and Devices Magazine*, 12 (5), 49 –50 (1996).
20. F. Bilodeau, D. C. Johnson, S. Theriault, B. Malo, J. Albert, and K. O. Hill, "An all-fiber dense-wavelength-division multiplexer/demultiplexer using photoimprinted Bragg gratings," *IEEE Photon. Technol. Lett.* **7**, 388-390 (1995).
21. I. Baumann, J. Seifert, W. Nowak, and M. Sauer, "Compact all-fiber add-drop-multiplexer using fiber Bragg gratings," *IEEE Photonics Technology Letters* **8**, 1331-1333 (1996).
22. Yoshinori Hibino, "High contrast waveguide devices," *Optical Fiber Communication Conference*, Paper **WB1-1**, Anaheim, California, March 17-22, 2001
23. Y. Hida, Y. Hibino, T. Kitoh, Y. Inoue, M. Itoh. T. Shibata, A. Sugita, and A. Himeno, "400-channel 25-GHz spacing arrayed-waveguide grating covering a

- full range of C- and L-bands,” *Optical Fiber Communication Conference*, Paper **WB2-1**, Anaheim, California, March 17-22, 2001
24. M. Oguma, T. Kitoh, K. Jinguji, T. Shibata, A. Himeno and Y. Hibino, “Flat-top and low-loss WDM filter composed of lattice-form interleaved filter and arrayed-waveguide gratings on one chip,” *Optical Fiber Communication Conference, 2001*. **3**. wb3-1 - wb3-3. (2001) .
 25. P. D. Trinh, S. Yegnanarayanan, F. Copping, B. Jalali, “Silicon-on-insulator phased-array waveguide grating WDM filter,” *Optical Fiber Communication Conference, OFC 97*, 301 –302 (1997)
 26. Wenhua Lin, Haifeng Li, Chen, Y.J., M. Dagenais, D. Stone, “Dual-channel-spacing phased-array waveguide grating multi/demultiplexers,” *IEEE Photonics Technology Letters* , **8** (11), 1501 –1503 (1996).
 27. Y. Inoue, A. Kaneko, F. Hanawa, H. Takahashi, K. Hattori, S. Sumida, “Athermal silica-based arrayed-waveguide grating multiplexer,” *Electronics Letters*, **33** (23), 1945-1947 (1997)
 28. C. G. M. Vreeburg, *et al.*, "A low-loss 16-channel polarization dispersion-compensated PHASAR demultiplexer," *IEEE Photon. Technol. Lett.* **10**, 382-384 (1998).
 29. Jie Qiao, Feng Zhao, James W. Horwitz, Ray T. Chen, “32 Channel 100GHz Spaced Demultiplexer for Metropolitan Area Network,” *Optical Engineering*, **40** (7), 1255-1299 (2001)

30. Feng Zhao, Jie Qiao, Xuegong Deng, Jizuo Zou, Baoping Guo, Ray Collins, Victor Villavicencio, Kwei K. Chang, Janmes W. Horwitz, Bill Morey, Ray T. Chen, “ Reliable grating-based wavelength division (de)multiplexers for optical networks,” *Optical Engineering*, **40** (7), 1204-1211 (2001)
31. George J. Cannell, Alex Robertson, Robin Worthington, “Practical realization of a high density diode-coupled wavelength demultiplexer,” *IEEE Journal of selected areas in communications*, **8** (6), 1141-1145 (1990)
32. J.P. Laude, I. Long, D. Fessard, “Low loss, low crosstalk M*N passive wavelength routers based on diffraction gratings ,” Lasers and Electro-Optics Society Annual Meeting, 1997. *LEOS '97 10th Annual Meeting. Conference Proceedings, IEEE*, **2**, 506 -507 (1996)
33. Philippe Martin, Bernard Laloux, Villepreux, Bertrand Merigot, Herve Lefevre, “Optical fiber wavelength multiplexer and demultiplexer,” Unite States Patent, Patent number 6,084,695
34. Stamatios V. Kartalopoulos, *Introduction to DWDM technology: Data in rainbow*, Bellingham, Wash.(1999).
35. Jerry Bautista and Robert Shine, “Filter technologies vie for DWDM system applications,”

www.fiberopticonline.com/content/news/article.asp?DocID={CA3F5DC1-4843-11D4-8C54-009027DE0829}
36. R.R. A.Syms, *Practical Volume Holography*, Clarendon Press, Oxford (1990).

37. M. G. Moharam and T.K. Gaylord, "Rigorous coupled-wave analysis of planar-grating diffraction," *J. Opt. Soc. Am.*, **71** (7), 811-818 (1981).
38. E. J. Restall, A.C. Walker, "Rigorous coupled-wave method applied to fan-out gratings," *IEE Proc. Optoelectron.*, Vol. **145**, No. 3, June 1998, p165-169 (1998).
39. H. Kogelnik, "Coupled wave theory for thick hologram gratings," *The Bell Sys. Tech. J.* **13**. 2909-2947 (1969).
40. Jian Liu, *Multi-wavelength planar optoelectronic interconnections*, Ph.D. Diss., The University of Texas at Austin, (1999).
41. W. Gambogi, K. Steijn, S. Mackara, T. Duzik, B. Hamzavy, and J. Kelly, "HOE imaging in DuPont holographic photopolymers," *Proc. SPIE* **2152**, 282-293 (1994).
42. U. Rhee, H. J. Caulfield, C. S. Vikram, and J. Shamir, "Dynamics of hologram recording in DuPont photopolymer," *Appl. Opt.* **34**, 846-853 (1995).
43. S. Piazzolla and B. K. Jenkins, "Holographic grating formation in photopolymers," *Opt. Lett.* **21**, 1075-1077 (1996).
44. H. J. Zhou, V. Morozov, and J. Neff, "Characterization of DuPont photopolymers in infrared light for free-space optical interconnects," *Appl. Opt.* **34**, 7457-7459 (1995).
45. Feng Zhao, Xuegong Deng, Jie Qiao, Jizuo Zou, Ray T. Chen "Chirp gratings for dense WD(D)M and optoelectronic interconnect applications" *Proceedings of SPIE* **3949**, 62-70 (2000)

46. R.R.A.Syms, "Vector effects in holographic optical elements," *OPTICA ACTA*, 1985, **32** (11), 1413-1425 (1985).
47. Alexander Stavdas, Polina Bayvel, John E. Midwinter, "Design and performance of concave holographic gratings for applications as multiplexers/demultiplexers for wavelength routed optical networks," *Opt. Eng.* **35**(10), 2816-2823 (1996).
48. Michael R. Wang, Tomasz Jansson, G.J. Sonek, "Substrate wavelength-demultiplexing optical interconnects based on superimposed holographic gratings and three-dimensional Bragg diffraction," *Optics Letters*, **18** (23), 2068-2070 (1993).
49. Jun-Won An, Nam Kim, Kwon-Yeon Lee, "Dynamic passband filter using converging wave and amplitude masks in holographic volume grating," *Electronics Letters*, **36** (25), 2092-2093 (2000)
50. M. Moulavi-Kakhki, M. Kavehrad, "Holographic optical filters and cross-talk performance in WDM networks," *Journal of Optical Communications*, **16** (5), 190-193 (1995)
51. E.G. Churin, P. Bayver, "Design of free-space WDM router based on holographic concave grating," *IEEE Photonics Technology Letters*, **11** (2), 221-223 (1999)
52. T. Jansson, "Holographic planar optical interconnects," *Proceedings of SPIE - 1990 International Topical Meeting on Optical Computing OC '90*, Apr 8-12 1990, 305-306 (1990)

53. Jian Liu and Ray T. Chen, "Path-reversed photopolymer-based substrate-guided-wave optical interconnects for wavelength division demultiplexing," *Applied Optics*, **38** (14) (1999)
54. Jie Qiao, Feng Zhao, Jian Liu, and Ray T. Chen, "Dispersion-enhanced Volume Hologram for Dense Wavelength-Division Demultiplexer," *IEEE Photonics Technology Letters*, **12**,1070-1072, 2000
55. Constantina Poga, Robert Blomquist, Louay Eldora, Robert A. Norwood, "Polymer Bragg gratings for wavelength division multiplexers," *Proceedings of SPIE*, **3633**, 81-91(1999)
56. X. Deng, F. Zhao, Zhenhai Fu, Jizuo Zou, Jie Qiao, G. Kim, Ray T. Chen, "Linearity of volume hologram out-coupling for wavelength-divisiondemultiplexing," *Proceedings of SPIE* **3949**, 109-119 (2000).
57. X. Deng, D. An, F. Zhao and Ray Chen, "Temperature sensitivity of passive holographic wavelength division multiplexers/demultiplexers," *Applied Optics*, **39**(23), 4047-4057 (2000).
58. Jian Liu and Ray T. Chen, "A two-dimensional dual-wavelength routing network with 1-to-10 cascaded fanouts," *IEEE Photonics Technology Letters*, **10**, 238-240 (1997).
59. Jian Liu, Chunhe Zhao, R. Lee, and Ray T. Chen, "Cross-link optimized cascaded volume hologram array with energy-equalized one-to-many surface-normal fan-outs," *Opt. Lett.* **22**, 1024-1026 (1997).

60. M. M. Li and R. T. Chen, "Five-channel surface-normal wavelength-division demultiplexer using substrate-guided waves in conjunction with a polymer-based Littrow hologram," *Opt. Lett.* **20**, 797-799 (1995).
61. Y. K. Tsai, Y. T. Huang, and D. C. Su, "Multiband wavelength-division demultiplexing with a cascaded substrate-mode grating structure," *Appl. Opt.* **34**, 5582-5588 (1995).
62. Jian Liu and Ray T. Chen, "Substrate-guided-wave-based optical interconnects for multi-wavelength routing and distribution networks," *Journal of Lightwave Technology*, **17**, 354-361(1999).
63. L.A. Bergman, J.Morookian, and C. Yeh, "WDM Component Requirements for Bit-Parallel Fiber Optic Computer Networks,"(unpublished, Dec. 1997)
64. J. E. Ludman, "Approximate bandwidth and diffraction efficiency in thick holograms," *Am. J. Phys.* **50**, 244-246 (1982).
65. T.Niewulis, "Accessible fiber to the last mile," in Proc. symp. Optical Internet 2000. Dallas, TX, Jan. 18-20, 2000.
66. U.Menzel. A. Barwolff. P. Enders, D. Ackermann, R.Puchert, and M. Voss, *Semicond. Sci. Technol.* **10**, 1382 (1995)
67. P. Bhattacharya. *Semiconductor Optoelectronic Devices* (Prentice-Hall, New Jersey, 323 (1994)

68. W. Gambogi, K. Steijn, S. Mackara, T. Duzik, B. Hamzavy, and J. Kelly, "HOE imaging in duPont holographic photopolymers," *Proc. Of SPIE* **2152**, 282-293 (1994)
69. H. J. Zhou, V. Morozov, and J. Neff, "Characterization of DuPont Photopolymers in infrared light for free-space optical interconnects," *Appl. Opt.* **34**, 7457-7459 (1995)"
70. Casimer DeCusatis, "Optical Data Communication: Fundamentals and Future Directions," *Optical Engineering*, **37** (12), 3082-3099 (1998)
71. R.R Patel, H.E. Garrett, M.A. Emanuel, M.C. Larson, M.D. Pocha, D.M. Krol, R.J. Deri and M.E. Lowry: 'WDM filter modules in compact, low-cost plastic packages for byte-wide multimode fiber ribbon cable data links' *Electronics Letters*, **35** (10), 840-841 (1999)
72. B. E. Lemoff, L. B. Aronson, and L. A. Buckman, "Zigzag waveguide demultiplexer for multimode WDM LAN," *Electronics Letters*, **34**, 1014-1016 (1998).
73. Lewis B. Aronson, Brian E. Lemoff, Lisa A. Buckman, " Low-cost multimode WDM for local area networks up to 10Gb/s," *IEEE Photonics Technology Letters*, **10** (10), 1489-1491 (1998).
74. Syn-Yem Hu, Jack Ko, Eric R. Hegblom, and Larry A. Coldren, "Multimode WDM optical data links with monolithically integrated multiple-channel VCSEL and photodetector arrays," *IEEE of Quantum Electronics*, **34** (8), 1403-1414 (1998).

75. Masafumi Koga and Takao Matsumoto, "A novel optical WDM demultiplexer consisting of a simple optical multimode guide and an electrical neural network," *IEEE Photonics Technology Letters*, **2** (7), 487-489 (1990)
76. W. J. Tomlinson, "Wavelength multiplexing in multimode optical fibers," *Appl. Opt.* **16**, 2180-2194 (1977).
77. R.C. Lasky, U.L. Osterberg, and D.P. Stigliani, *Optoelectronics for Data Communications*, New York: Academic (1995)
78. Jie Qiao, Feng Zhao, and Ray T. Chen, William W. Morey, James W. Horwitz, Ray Collins, George Chang, and Victor Villavicencio, "Multimode 200 GHz-spaced dense wavelength division demultiplexing for local area networks," *Proceedings of SPIE* **4289**, 52-58 (2001)
79. Kanabar, Y.; Baker, N.; Cannell, G.J.; Robertson, A.J. "High density wavelength division multiplexing for multiple access networks," *Optical Multiple Access Networks, IEE Colloquium on 1991*, 9/1-9/4 (1991)
80. E. Loewen, D. Maystre, E. Popov, and L. Tsonev, "Echelles: scalar, electromagnetic, and real-groove properties," *Applied Optics*, **34** (10), 1707-1727 (1995).
81. E. Loewen, D. Maystre, E. Popov, and L. Tsonev, "Diffraction efficiency of echelles working in extremely high orders," *Applied Optics*, **35** (10), 1700-1704 (1996).

82. Yohji Fujii, Kou-ichi Aoyama, and Jun-ichiro Minowa, "Optical demultiplexer using a silicon echelette grating," *IEEE Journal of Quantum Electronics*, **QE-16** (2), 165-169 (1980)
83. M.S.D. Smith and K.A. McGreer, "Diffraction gratings utilizing total internal reflection facets in Littrow configuration," *IEEE Photonics Technology Letters*, **11** (1), 84-86 (1999).
84. M. Collischon, H. Haidner, P. Kipfer, A. Lang, J.T. Seridan, J.Schwider, N. Streibl, and J.Lindolf, "Binary blazed reflection gratings," *Applied Optics*, **33**(16), 3572-3577 (1994).
85. R.D. Boyd, J.A. Britten, D.E. Decker, B.W. Shore, B.C. Stuart, M.D. perry, and Lifeng Li, "High-efficiency metallic diffraction gratings for laser applications," *Applied Optics*, **34** (10), 1967-1705 (1995).
86. M.C. Hutley, *Diffraction Gratings*, 35, Academic Press, New York, New York (1982)
87. Erwin G. Loewen, Evgeny Popov, *Diffraction gratings and applications*, Marcel Dekker, Inc., New York, New York (1997)
88. "Schott Optical Glass," Schott Glass Technologies, Duryea, PA, (1992)
89. J.P.Laude, *Wavelength Division Multiplexing*, Prentice Hall (1993)
90. Telecommunication Standardization Sector of the International Telecommunication Union (ITU-T), Place des nations, CH-1211 Geneva 20, Switzerland (<http://www.itu.ch>).

91. A. McGuire and P. Bonenfant, "Standards: The blueprint for optical networking," *IEEE Commun. Mag.*, **36**, 68-75 (1998).
92. R.E. Wagner and W.J. Tomlinson, "Coupling efficiency of optics in single-mode fiber components," *Applied Optics*, **21** (15), 2671-2688 (1982).
93. C.M. Miller and S.C. Mettler, "A loss model for parabolic-profile fiber splices," *The Bell System Technical Journal*, **57** (9), 3167-3180 (1978)
94. E.G. Churin and P. Bayvel, "Pass band flattening and broadening techniques for high spectral efficiency wavelength demultiplexers," *Electronics Letters*, **35** (1), 27-28 (1999)
95. C. Dragone, T. Strasser, G.A. Bogert, L.W. Stulz P. Chou, "Waveguide grating router with maximally flat passband produced by spatial filtering," *Electronics Letters*, **33** (15), 1312 –1314 (1997)
96. A.Rigny, A.Bruno, H. Sik, "Multigrating method for flattened spectral response wavelength multi/demultiplexer," *Electronics Letters*, **33** (20), 1701 –1702 (1997)
97. C.P.Botham, "Theory of tapering single-mode optical fibres by controlled core diffusion," *Electronics Letters*, **24** (4), 243-244 (1988)
98. J.S Harper, C.P.Botham; S. Hornung, "Tapers in single-mode optical fibre by controlled core diffusion," *Electronics Letters*, **24** (4), 245-246 (1988)
99. Duncan T. Moore, "Gradient-index optics: a review," *Applied Optics*, **19**(7), 1035-1043 (1980).
100. Kazou Shiraishi, Akira Ogura, and Kota Matsuura, "Spotsize contraction in

- standard single-mode fibers by use of a GI-fiber tip with a high focusing parameter,” *IEEE Photonics Technology Letters*, **10** (12), 1757-1759 (1998)
101. W. Bludau and R. Rossberg, “Low-loss laser-to-fiber coupling with negligible optical feedback,” *Journal of Lightwave Technology*, **LT-3**, 294-302 (1985)
 102. Kazuo Shiraishi, “A new lensed-fiber configuration employing cascaded GI-fiber chips,” *Journal of Lightwave Technology*, **18**(6), 787-794 (2000).
 103. J. Laude and K. Lange, “Dense wavelength division multiplexer and routers using diffraction grating,” *Proc. of NFOEC 99*, **1**, 83-88 (1999)
 104. Jay Hirsh, Viken Y. Kalindjian, Freddie S. Lin, Michael R. Wang, Guoda Xu, Tomasz Jansson, “High channel density broadband wavelength division multiplexers based on periodic grating structures,” *SPIE* **2532**, 171-181 (1995).
 105. Herwig Kogelnik, “Imaging of optical modes – resonators with internal lenses,” *Bell System Technical Journal*, **44**, 455-495 (1965).
 106. William L. Emkey and Curtis A. Jack, “Analysis and evaluation of graded-index fiber-lenses,” *Journal of Lightwave Technology*, **LT-5** (9), 1156-1163 (1987)

Vita

Jie Qiao received her B.S. degree in Electrical Engineering in 1992, her MS degree in Precision Instrument and Mechanics in 1997 from Tsinghua University, China. In 2000 she received another MS degree in Electrical Engineering from the University of Texas at Austin. She worked as an electrical engineer in automatic control systems at Anshan Iron and Steel Cooperation, Anshan, China from 1992-1994.

Jie is currently an optical engineer at Radiant Photonics Inc. She has designed three grating-based demultiplexers with low insertion loss and low crosstalk. She submitted one patent disclosure on the passband broadening of grating-based WDM in 2001. Her research interests cover wavelength division multiplexers, optical networks, optoelectronic interconnects, variable optical attenuators, and optical switches.

Publications:

1. **Jie Qiao**, Feng Zhao, James W. Horwitz, Ray T. Chen, “32 Channel 100GHz Spaced Demultiplexer for Metropolitan Area Network” *Optical Engineering*, 40 (7), 1255-1299 (2001)
2. **Jie Qiao**, Feng Zhao, Jian liu, Ray T. Chen, ‘Dispersion-enhanced Volume Hologram for Dense Wavelength-Division Demultiplexer’ *IEEE Photonics Technology Letters*, 12 (8), 1070-1072 (2000)

3. Feng Zhao, **Jie Qiao**, Xuegong Deng, Jizuo Zou, Baoping Guo, Ray Collins, Victor Villavicencio, Kwei K. Chang, Janmes W. Horwitz, Bill Morey, Ray T. Chen, “ Reliable grating-based wavelength division (de)multiplexers for optical networks,” *Optical Engineering*, 40 (7), 1204-1211 (2001)
4. **Jie Qiao**, Feng Zhao, Ray T. Chen, William W. Morey, James W. Horwitz, Ray Collins, George Chang, and Victor Villavicencio, “Multimode 200 GHz-spaced dense wavelength division demultiplexing for local area networks,” *Proceedings of SPIE*, 4289, 52-58 (2001)
5. **Jie Qiao**, Feng Zhao, Jian Liu, Ray T. Chen, “Fully packaged dense wavelength division demultiplexer for optical networks”, *Proceedings of SPIE* 3949, 71-80 (2000)
6. Feng Zhao, Xuegong Deng, **Jie Qiao**, Jizuo Zou, Ray T. Chen “Chirp gratings for dense WD(D)M and optoelectronic interconnect applications” *Proceedings of SPIE* 3949, 62-70 (2000)
7. James W Horwitz, Xuegong Deng, Al Morgan, **Jie Qiao**, Victor Villavicencio, Feng Zhao, Jizuo Zou, Ray T. Chen, “Highly reliable 32-channel wavelength division demultiplexer,” *Proceedings of SPIE* 3949, 82-89 (2000)
8. Xuegong Deng, Feng Zhao, Zhenhai Fu, Jizuo Zou, **Jie Qiao**, G. Kim, Ray T, Chen “Linearity of volume hologram out-coupling for wavelength-division demultiplexing ” *Proceedings of SPIE*, 3949, 109-119 (2000)

9. Jian Liu, **Jie Qiao**, Ray T. Chen, Davies, Brian M. “Multi-mode dense WDDM for data communications” *LEOS Summer Topical Meeting Jul 26-Jul 27 1999*, 53-54,1099-4724 (1999).

Permanent address: 4410 Ave F. 101B, Austin, TX, 78751

Jie Qiao typed this dissertation.